# UC San Diego

## UC San Diego Electronic Theses and Dissertations

**Title**

Application of infrared nanooptics to ultrathin materials

**Permalink**

https://escholarship.org/uc/item/18g6k6d6

**Author**

Andreev, Gregory

**Publication Date**

2011

Peer reviewed|Thesis/dissertation

eScholarship.org Powered by the California Digital Library
University of California

UNIVERSITY OF CALIFORNIA, SAN DIEGO

# Application of Infrared Nanooptics to Ultrathin Materials

A dissertation submitted in partial satisfaction of the
requirements for the degree
Doctor of Philosophy

in

Physics

by

Gregory Andreev

Committee in charge:

Professor Dimitri N. Basov, Chair
Professor Massimiliano Di Ventra
Professor Shaya Fainman
Professor Michael Fogler
Professor Shayan Mookherjea

2011

Copyright
Gregory Andreev, 2011
All rights reserved.

The dissertation of Gregory Andreev is approved, and it is acceptable in quality and form for publication on microfilm and electronically:

_____

_____

_____

_____

_____

Chair

University of California, San Diego

2011

DEDICATION

To those that carry the fire.

# EPIGRAPH

*We do not know where we are stupid unless we stick our neck out.*

—Richard Feynman

TABLE OF CONTENTS

LIST OF FIGURES

LIST OF TABLES

ACKNOWLEDGEMENTS

As a graduate student at UCSD I was influenced most by those who pushed me to excel. The person that did that best was of course my advisor, Dimitri Basov. Despite a slow start, in the end the results of our collaboration turned out extremely fruitful. We built the world's first cryogenic infrared nanoscope, made the first observation of a massless Dirac plasmon and also discovered a new quasiparticle (which we have yet to name): a phonon coupled to a massless plasmon. Dimitri motivated me to take the right chances and push the limits of my creativity. I am grateful for this life changing opportunity.

I would also like to acknowledge my friends and colleagues, especially Tom Driscoll, Alex McLeod, and Erik Shipton who are not only great physicists but also fun to have a drink with. I would like to thank Zhe Fei, Misha Fogler and Matt Zhang for all their hard work and insight for our Graphene project. Also, I extend my gratitude to Fritz Keilmann, Rainer Hillenbrand, Andy Huber, Nenad Ocelic, Markus Brehm and everyone else from Neaspec for helping me learn the basics of sSNOM early on in my studies. In addition, I'm grateful to all of my collaborators on the published and soon-to-be published works in this thesis:

T. Driscoll, G. O. Andreev, D. N. Basov, S. Palit, S. Y. Cho, N. M. Jokerst, and D. R. Smith. "Tuned permeability in terahertz split-ring resonators for devices and sensors". Applied Physics Letters, 91(6):062511, 2007 (appearing in Chapter 1),

Z. Fei, G. O. Andreev, W. Bao, L. M. Zhang, Z. Zhao, G. Dominguez, M. Thiemens, M. M. Fogler, C. N. Lau, F. Keilmann, and D. N. Basov. "Dirac plasmons at the graphene-SiO2 interface". (submitted), 2011. (appearing in Chapter 2),

G. O. Andreev, Z. Fei, A. S. McLeod, W. Bao, L. M. Zhang, A. Castro-Neto, Z. Zhao, G. Dominguez, M. Thiemens, M. M. Fogler, C. N. Lau, F. Keilmann, and D. N. Basov. "Infrared nanooptics of ultrathin materials." (in preparation), 2011. (appearing in Chapter 3).

I have to thank my family for sticking through with me during this 8 year journey of student loans, long distance phone calls and countless hours of stress. My father especially, who was always there for me no matter what.

Last but not least, I have to mention my girlfriend Nikki, who I met during my

last year in San Diego. While I never intended to stay here for so long, she makes a damn good reason for having done so. Otherwise I would not be with the most wonderful, understanding, and beautiful woman on the planet. Who else would bring me a burrito and two beers during yet another midnight data run?

## VITA

| | |
|---|---|
| 2003 | B. S. in Physics and Mathematics *summa cum laude*, University of Texas at Austin |
| 2003-2011 | Research Assistant, University of California, San Diego |
| 2005 | MS. in Physics, University of California, San Diego |
| 2011 | Ph. D. in Physics, University of California, San Diego |

## PUBLICATIONS


G. O. Andreev, Z. Fei, A. S. McLeod, W. Bao, L. M. Zhang, A. Castro-Neto, Z. Zhao, G. Dominguez, M. Thiemens, M. M. Fogler, C. N. Lau, F. Keilmann, and D. N. Basov. "Infrared nanooptics of ultrathin materials." (in preparation), 2011.

Z. Fei, G. O. Andreev, W. Bao, L. M. Zhang, Z. Zhao, G. Dominguez, M. Thiemens, M. M. Fogler, C. N. Lau, F. Keilmann, and D. N. Basov. "Dirac plasmons at the graphene-SiO2 interface". (submitted) 2011.

T. Driscoll, G. O. Andreev, D. N. Basov, S. Palit, S. Y. Cho, N. M. Jokerst, and D. R. Smith. "Tuned permeability in terahertz split-ring resonators for devices and sensors." Applied Physics Letters, 91(6):062511, 2007.

M. Qazilbash, M. Brehm, G. O. Andreev, A. Frenzel, P. C. Ho, B. G. Chae, B. J. Kim, S. J. Yun, H. T. Kim, A. Balatsky, O. Shpyrko, B. Maple, F. Keilmann, and D. N. Basov. "Infrared spectroscopy and nano-imaging of the insulator-to-metal transition in vanadium dioxide". Physical Review B 79.7 (2009).

T. Driscoll, G. O. Andreev, D. N. Basov, S. Palit, T. Ren, J. Mock, S. Y. Cho, N. M. Jokerst, and D. R. Smith. "Quantitative investigation of a terahertz artificial magnetic resonance using oblique angle spectroscopy". Applied Physics Letters 90.9 (2007), p. 092508.

T. Driscoll, G. O. Andreev, D. N. Basov, S. Palit, S. Y. Cho, N. M. Jokerst, and D. R. Smith. "Tuned permeability in terahertz split-ring resonators for devices and sensors". Applied Physics Letters 91.6, 062511 (2007), p. 062511.

M. M. Qazilbash, M. Brehm, B. G. Chae, P. C. Ho, G. O. Andreev, B. J. Kim, S. J. Yun, A. V. Balatsky, M. B. Maple, F. Keilmann, H. T. Kim, and D. N. Basov. "Mott Transition in VO2 Revealed by Infrared Spectroscopy and Nano-Imaging". Science 318.5857 (2007), p. 1750.

A. T. Hammack, N. A. Gippius, Sen Y., G. O. Andreev, L. V. Butov, M. Hanson, and A. C. Gossard. ”Excitons in electrostatic traps”. Journal of Applied Physics 99.6 (2006), p. 066104.

ABSTRACT OF THE DISSERTATION

**Application of Infrared Nanooptics to Ultrathin Materials**

by

Gregory Andreev

Doctor of Philosophy in Physics

University of California, San Diego, 2011

Professor Dimitri N. Basov, Chair

My thesis describes the study of nanoscale physics using infrared spectroscopy and nanoscopy methods. The first phase of my research was the development of new methods for tuning metamaterials, which possess custom tailored optical properties not easily found in nature. Working together with Tom Driscoll, I co-invented a simple yet effective method for tuning the magnetic permeability of a Split Ring Resonator based metamaterial. This is the topic of Chapter 1. My subsequent research dealt with near field optics, in particular the application of the infrared imaging method of scattering Scanning Nearfield Optical Microscopy to ultrathin materials such as single layer Graphene and $2nm$ thin $SiO_2$ layers on Silicon. On both of these materials we demonstrated incredible sensitivity to $\leq 10 \times 10 \times 1nm^3$ volumes (Chapter 3). Thanks to the incredibly large momenta of the evanescent light utilized in sSNOM, we also discovered

a rich array of previously unobserved physics in Graphene. In particular, we were able to observe the resonance enhancement of the $SiO_2$ phonon by the presence of plasmon oscillations in Graphene (Chapter 2). Lastly, a large part of my thesis work also involved building the first cryogenic sSNOM with which we were able to directly image the metal to insulator transition in the correlated oxide: $V_2O_3$, shown in the last chapter.

# 1 Tuned permeability in Terahertz Split-Ring Resonators for devices and sensors

## 1.1 Abstract

A process is demonstrated for tuning the magnetic resonance frequency of a fixed Split-Ring resonator array, by way of adding material near the split-ring elements. Applying drops of a silicon-nanospheres/ethanol solution to the surface of the sample decreases the magnetic resonance frequency of the Split-Ring array in incremental steps of 0.03 THz. This fine tuning is done post-fabrication, and is demonstrated to be reversible. The exhibited sensitivity of the Split-Ring resonance frequency to the presence of silicon nanospheres also suggests further application possibilities as a sensor device.

## 1.2 Introduction

Device design is quickly becoming a large part of metamaterial research. In the short half-decade since its conception, understanding of the physics behind tailored electromagnetic responses in metamaterials has progressed far enough to where application demonstrations are surfacing. Prime examples include diffraction beating lenses [1, 2], frequency selective cloaks [3, 4, 5], advanced optics [6, 7], and improved radomes [8]. Many of these devices have been demonstrated at the microwave frequencies, aided by the comparable ease of fabricating millimeter scale structures. Operation at higher fre-

quencies – infrared and above – requires smaller structures which are usually patterned photo-lithographically [9, 10]. The photo-lithographic step is often a hurdle to creating infrared devices, as it requires designing and purchasing an expensive lithography mask – which then permanently fixes the metamaterial structures. To make matters more difficult, design methods rely on finite-element or similar numerical solvers; so even the best efforts in design can incorrectly predict the resonant response frequency of a structure by 5%.

## 1.3 Experimental details

Given all these considerations, it is clear that there is significant utility in developing the ability to alter the response of any metamaterial structure without the need to design a new lithography mask. Active tuning based on modification of the electromagnetic properties of materials is one option being pursued [11], with clear advantages for switchable devices [12]. Despite advantages, the architecture of initial active-tunable devices has been quite complicated, and the tunable frequency range limited. In this letter, we demonstrate a simple procedure for passive tuning of a Split-Ring Resonator (SRR) response. Although the tuning process is certainly not limited to SRRs, we consider them exclusively here for simplicity and familiarity [13]. We use the same SRR array as in the work of Ref. [13], wherein gold SRRs are patterned on a 1 mm thick Silicon substrate coated with a thin 6 $\mu$m layer of BenzoCycloButane (BCB). The BCB is used as a low-loss adhesive aid in performing the gold lithography. A photograph of this SRR array is shown in Fig. 1.1a. This metamaterial is designed to have a magnetic resonance at 1.20 THz, which experimentally manifests as a sharp dip in sample transmission, shown in Fig. 1.2 as the black curve. Transmission is probed in a FTIR spectrometer using s-polarized 45$^\circ$ incident light (see insert in Fig. 1.3). The details of this style of measurement, and a more in depth discussion of how this dip is known to be the magnetic mode of the SRR, can be found in Refs. [13, 14]. One improvement on the method in Ref. [13] is explored in this work: sample transmission spectra exhibit large Fabry-Perot fringes which arise from multiple reflections within the thick 1 mm silicon substrate. These fringes make precise determination of the resonance frequency

difficult. The fringes have a known periodicity which is set by the thickness of the substrate, so in our analysis we pass the transmission spectra through a digital notch-filter which removes the fringes. Because the notch filter is sharply targeted at the substrate fringes, no other features of the spectra are significantly affected.

## 1.4 Passive tuning of the SRR

Passive tuning in this letter is accomplished by adding dielectric material to alter the capacitance of the SRR. A simplified model of the SRR can be thought of as an inductive-capacitive [15, 16]. The self-inductance of each loop battles the capacitance of the split-gap to determine the resonance frequency (and all other attributes of the resonance) following

$$\omega_0 \propto \frac{1}{\sqrt{LC}} = \frac{1}{\sqrt{L}\sqrt{\varepsilon_0 \int^{v} \varepsilon(v) E(v) dv}} \tag{1.1}$$

The electric field falls off quickly away from the metamaterial layer so the volume integral need only be considered in vicinity of the SRR. Cross-sections of the electric field distribution for our SRR are displayed in Fig. 1.1g, as solved by finite-integration time-domain solver. The high intensity of the electric field $\mathbf{E}(v)$ in the gap region makes the resonance frequency sensitive to small changes in the dielectric $\varepsilon$. To take advantage of this, we prepare a 0.2% solution of silicon nanospheres (50 nm diameter – prepared by weight), suspended in ethanol using an ultrasonicator. The solution is then applied to the surface of our sample in small drops of 30 $\mu$l (average drop volume as measured by weight). The sample is heated to 60°C, so shortly upon contact with the sample the ethanol evaporates leaving behind only the silicon nanospheres. This procedure produces a fairly uniform layer (a video of this puddle application and drying process is made available online at physics.ucsd.edu/ tdriscol/SiPuddle.mpeg). Figure 1.1b shows a photograph of the SRR array after this first application. The introduction of the silicon material onto the SRR effectively increases the capacitance and thus decreases the resonant frequency, and we observe that the transmission dip decreases by $\sim$0.05 THz (Fig. 1.2, blue curve). Repeated applications of 30 $\mu$l drops of this solution deposit additional silicon spheres (pictured in Fig. 1.2c–e) which continue to decrease

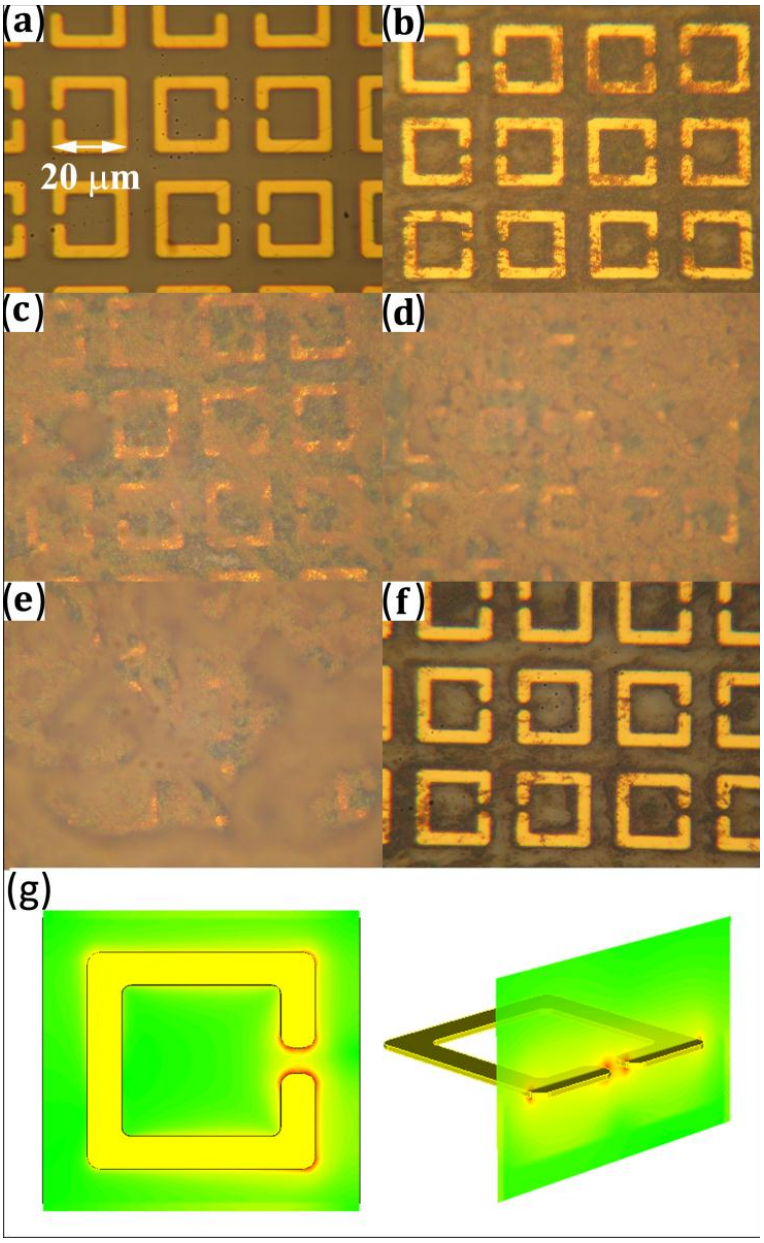


**Figure 1.1**: Photographs of the gradual addition of silicon nanospheres by solution. Panel (f) shows the sample after removing most of the silicon by ultrasonics. Panel (g) shows cross-sections of the electric field intensity (solved by finite-integration time-domain). The scale is logorithmic, green is the incident field intensity, red is 100× incident.

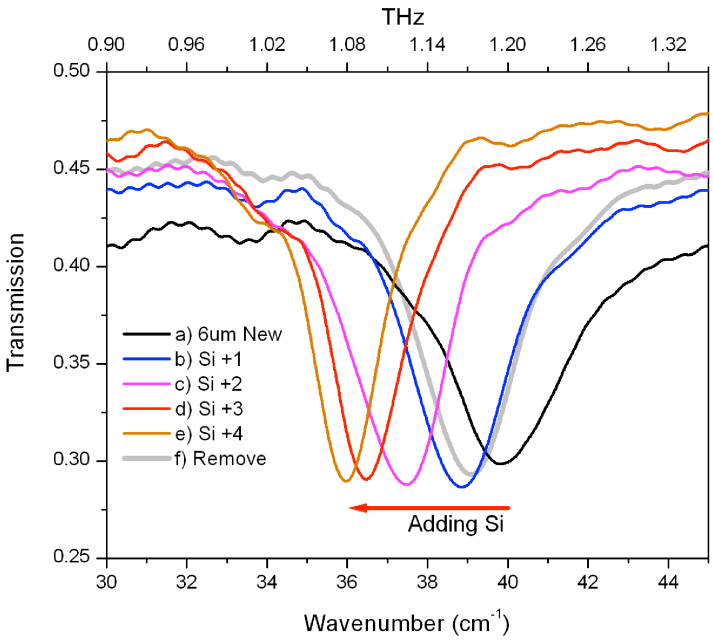


**Figure 1.2**: Fine tuning: Addition of silicon nanospheres increases the average dielectric of the SRR capacitance and shifts the magnetic resonant frequency downwards. Thick grey (line f) shows near-restoration of the original response by removal of the nanospheres in an ultrasonicator.

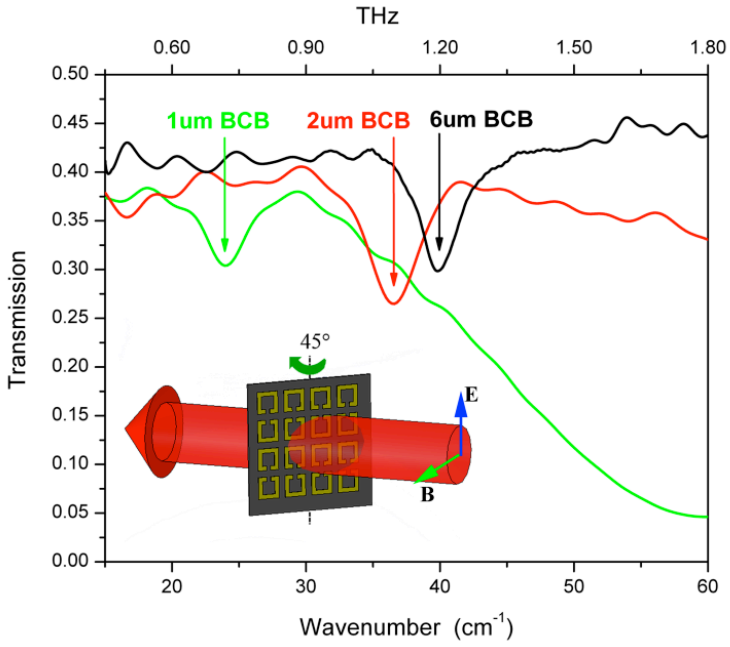


**Figure 1.3**: Coarse tuning: Three values of the BCB spacer thickness showing thinner spacers decrease the SRR magnetic resonance position.

the resonance in steps. Saturation of this effect begins by picture/line f, and further applications reduce the resonance frequency in diminishing increments. A weaker solution of nanospheres could presumably give even finer step-sizes, and an exact resonance frequency can be created via a guess and check methodology. Another interesting effect of the silicon addition is an observed sharpening and deepening of the magnetic resonance dip. This is qualitatively sensible, as the Q factor of a parallel RLC-circuit should increase with increasing capacitance. This sharpening is also an indicator that addition of the silicon nanospheres does not appreciably add to the damping of the SRR resonator (the nanospheres are nearly intrinsic silicon and so have a very small imaginary permittivity at THz).

The accumulation of the silicon spheres is also reversible. We briefly (30 seconds) submerge the sample in an ultrasonicated ethanol bath, and most of the silicon is removed (Fig. 1.2f). The resonance frequency also returns to nearly to its original position. Not entirely all of the spheres come off, we see that the spheres clustered near the edges of the SRRs remain. This reversibility is an important attribute; if the desired

resonant frequency is overshot we can reset and begin the application process anew.

The observed sensitivity of the SRR metamaterial resonance frequency to the introduction of microliters of our weak solution of silicon nanoparticles also brings to mind the possibility of using such devices as sensors. The 30 $\mu$l drop contains an amount of silicon so small (less than 1 nanogram) that we cannot detect it via standard transmission-amplitude experiment [1]. The Silicon layer which we add to the SRRs is many times thinner than the skin depth of THz radiation. Using our SRR array as a probe offers a significant advantage, as we transform detection of the silicon nanospheres from a transmission-amplitude level measurement to a resonance frequency position measurement, which is often much more accurate [17]. The resonance frequency of the SRR is sensitive to very small quantities of material as the concentrated fields within the split-gap most strongly interrogate a volume of only $\sim 3\mu\text{m}^3$. The field concentration increases with increasing $Q$-factors, and for SRRs the $Q$ is generally around 10. A cleverly designed metamaterial sensor with high $Q$ might thus be able to detect quantities of material even several orders of magnitude less than that demonstrated in this letter, and we are in the process of designing and investigating such devices.

## 1.5 Outlook

Fine tuning by addition of silicon nanospheres gives control over the resonance frequency to within a change of $\sim$10%, as we see in Fig. 1.2. We can effectively extend this tuning range by also varying the thickness of the BCB spacer used. Since BCB has a lower dielectric than silicon, a thinner BCB layer lets more of the SRR fields penetrate the silicon substrate, and lowers the resonance frequency. Fig. 1.3 demonstrates this, showing that using a thinner BCB layer creates a lower resonance frequency, acting as a method for coarse tuning. Imprecision in the BCB spin-coating process limits this coarse tuning to an accuracy of 5–10%, which meshes nicely with our fine tuning By combination of the coarse and fine tuning methods, we can feasibly create a metamaterial with a precise magnetic resonance frequency anywhere over the octave from 0.70 THz to 1.20 THz all without needing to change the feature sizes. Combined

[1] The amplitude change (as modeled in WVASE) from adding a 500 nm layer of Si spheres is less than 0.05 percent, below the noise level for this experiment.

with the possibility of sensors which probe sub-wavelength volumes, the sensitivity of metamaterials to passive material inclusions holds potential for interesting designs and applications.

## 1.6 Acknowledgements

The author would like to thank the co-authors of this publication for allowing its usage in this dissertation:

T. Driscoll, G. O. Andreev, D. N. Basov, S. Palit, S. Y. Cho, N. M. Jokerst, and D. R. Smith. ”Tuned permeability in terahertz split-ring resonators for devices and sensors”. Applied Physics Letters, 91(6):062511, 2007

# Bibliography


[1] N. Fang, H. Lee, C. Sun, and X. Zhang. *Science*, 308:534, 2005.

[2] D. R. Smith. *Science*, 308:502, 2005.

[3] J. B. Pendry, D. Schurig, and D. R. Smith. *Science*, 312:1780, 2006.

[4] D. Schurig, J. J. Mock, B. J. Justice, S. A. Cummer, J. B. Pendry, A. F. Starr, and D. R. Smith. *Science*, 314:977, 2006.

[5] Wenshan Cai, Uday K. Chettiar, Alexander V. Kildishev, and Vladimir M. Shalaev. Optical cloaking with non-magnetic metamaterials. *physics/*, page 0611242, 2006.

[6] T. Driscoll, D.N. Basov, A.F. Starr, P.M. Rye, S. Nemat-Nasser, D. Schurig, and D.R. Smith. *App. Phys. Lett.*, 88:081101, 2006.

[7] D. Schurig and D. R. Smith. *Phys. Rev. E*, 70:065601, 2004.

[8] H. Liu, H. Su, K. Lin, C. Wu, C. Tang, and S. Yeh. In *IEEE Antennas and propagation symposium*, pages 19–22. IEEE, 2006.

[9] T.J. Yen, W.J. Padilla, N. Fang, , D.C. Vier, D.R. Smith, J.B. Pendry, D.N. Basov, and X. Zhang. *Science*, 303:1494, 2004.

[10] W.J. Padilla, D.N. Basov, and D.R. Smith. *Materials Today*, 9:28, 2006.

[11] I. Gil, J. Garcia, J. Bonache, F. Martin, M. Sorolla, and R. Marques. *IEEE Electric Letters*, 40:1347–1348, 2004.

[12] Hou-Tong Chen, Willie J. Padilla, Joshua M. O. Zide, Arthur C. Gossard, Antoinette J. Taylor, and Richard D. Averitt. *Nature*, 444:597, 2006.

[13] T. Driscoll, G. O. Andreev, D. N. Basov, S. Palit, Tong Ren, Jack Mock, Sang-Yeon Cho, Nan Marie Jokerst, , and D. R. Smith. *Appl. Phys. Lett.*, 90:092508, 2007.

[14] T. Driscoll, D. N. Basov, W. J. Padilla, J. J. Mock, , and D. R. Smith. *Phys. Rev. B*, 75:115114, 2007.

[15] J.D. Baena, J. Bonache, F. Martin, R. M. Sillero, F Falcone, T. Lopetegi, M.A.G. Laso, J Garcia, I. Gil, M.F. Portillo, and M. Sorolla. *IEEE Trans Microwave Theory*, 53(4), 2005.

[16] G.V. Eleftheriades, O. Siddiqui, and A.K. Iyer. *IEEE Microwave and Wireless Lett.*, 13(2), 2003.

[17] M. Brucherseifer, M. Nagel, P. Haring Bolivar, H. Kurz, A. Bosserhoff, and R. Buttner. *App. Phys. Lett.*, 77(24):4049, 2000.

# 2 Infrared nanoscopy of Dirac plasmons at the graphene-SiO2 interface

## 2.1 Abstract

We report on novel optical phenomena associated with Dirac plasmons in graphene that we investigated by means of infrared (IR) nanoscopy. By confining radiation from mid-IR lasers at the apex of a nanoscale tip, we achieved two orders of magnitude increase in the value of in-plane wavevector $q$ imperative to probe plasmonic effects in graphene layer. At these high wavevectors, the Dirac plasmon is found to dramatically enhance the interaction of near-field light with $SiO_2$ substrate. Our data augmented by detailed modeling establish graphene as a new medium supporting plasmonic effects that can be controlled by gate voltage.

## 2.2 Introduction

Surface plasmons are fundamental collective modes of electrons that enable functionalities at the intersection of nanophotonics and electronics [1, 2, 3, 4]. Dirac plasmons of graphene, which is the density waves of Dirac fermions, are predicted to enable both low losses and efficient wave localization up to mid-infrared frequencies [5, 6, 7, 8, 9, 10]. Theoretical studies show that the combination of tunability and low losses is highly appealing for implementation of nanophotonics, optoelectronics, and

transformation optics based on Dirac plasmons [10, 11, 12]. So far, optical phenomena associated with Dirac surface plasmons of the massless quasi-particles in graphene have remained unexplored. This is in part due to the complexity of carrying out infrared experiments at wavevectors matching those of plasmons: parameter space beyond the reach of conventional transmission or reflection measurements [13]. To overcome this limitation, we employed scattering-type near-field nanoscopy. We identified spectroscopic signatures attributable to the Dirac plasmon and its interaction with the surface phonon of the $SiO_2$ substrate. Our work affirms the under-exploited capability of tip-based optical nanoscopy to probe collective charge modes far away from $q \approx 0$ of conventional optical spectroscopy.

## 2.3 Experimental detail

In our experiments, we utilized a *NeaSNOM* (neaspec.com) nanoscope coupled to several interchangeable lasers (two quantum cascade lasers from *Daylightsolutions* and two $CO_2$ lasers from *Access Laser Company*), which in combination cover the mid-IR region from 883 to 1270 $cm^{-1}$ (Figs 2.1, 2.2). This region accommodates characteristic features of the electromagnetic response of monolayer graphene [14] along with vibrational modes of $SiO_2$. The infrared nanoscope is built on the basis of an Atomic force microscope (AFM) in tapping mode. We acquired near-field images with tapping frequency $\Omega \sim 270$ kHz and tapping amplitude $\Delta z = 40$ nm at ambient. The back-scattered signal is demodulated at the 2nd, 3rd and 4th harmonics of the tapping frequency yielding background-free images [15]. The scattering amplitude $s$ and phase $\phi$ at all harmonics are obtained simultaneously with AFM topography by pseudo-heterodyne interferometric detection [16].

Figure 2.1a displays a schematics of the nanoscopy experiment. The beam of an infrared (IR) laser is focused on the metalized tip of an AFM cantilever. The strong near-field confinement of mid-IR radiation at the tip apex has two principal effects. First, the collection of back-scattered light from a confined volume characterized by the tip radius $a$ enables infrared imaging/spectroscopy deep in the sub-diffractional regime [15]. Second, the light-matter interaction induced at the vicinity of the tip peaks for

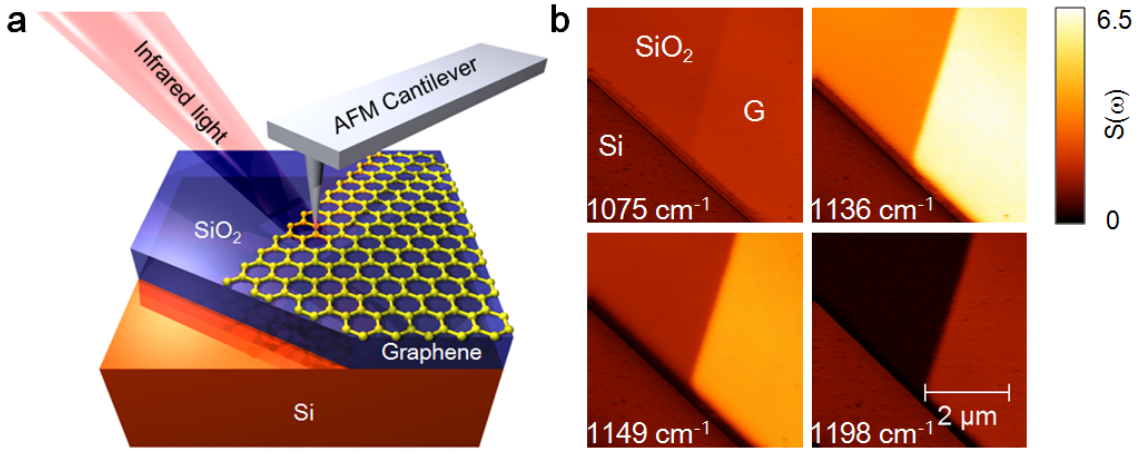


**Figure 2.1**: (a) Schematics of the near-field nanoscopy experiment used to study monolayer graphene on top of $SiO_2$/Si substrate. In the bottom left corner of the structure,$SiO_2$ has been etched through to enable tip contact with Si wafer. (b) Infrared near-field images displayed at four representative frequencies. The strong infrared contrast between Si, $SiO_2$ and graphene (G) is clearly seen to vary systematically with the probing frequency. The plotted quantity $s(\omega)$ is the normalized backscattering amplitude defined in the text.

in-plane momenta $q \approx 1/a$ , far beyond the light line given by $q = \omega/c$. It is this combination of sub-diffractional spatial resolution and high-$q$ coupling that enables us to investigate the spectroscopic signatures of Dirac plasmons by means of IR nanoscopy.

Graphene samples were fabricated by mechanical cleavage of graphite and then transferred to the surface of a 300 nm thick $SiO_2$ on a Si wafer. Raman spectroscopy was used to choose monolayer samples with identical hole-doping corresponding to a chemical potential of $\mu \sim (1800 \pm 200)$ cm$^{-1}$ and a carrier density of $n \sim (2.9 \pm 0.7) \times 10^{12}$ cm$^{-1}$ (see Supporting Information). For absolute spectroscopic measurements, we etched off $SiO_2$ in several regions of the wafer to access the near-field response of Si which is frequency-independent in the mid-IR region. Thus Si can serve as a convenient reference for a quantitative analysis of the nanoscale electrodynamics of graphene on $SiO_2$. For gating experiments, we fabricated electric contacts to the graphene surface.

In Fig. 2.1b we show representative IR nanoscopy images, in which we plot the backscattering amplitude normalized to Si: $s(\omega) = s_3(\omega)/s_3^{Si}(\omega)$ . Here, the backscat-

tering amplitude $s_3(\omega)$ is demodulated at the 3rd harmonic of the tip tapping frequency. The simultaneously recorded AFM topography is displayed in Fig. S1 in the Supporting Information. These images reveal nearly uniform signals in either $SiO_2$ or graphene regions with characteristics varying systematically with IR frequency. In Fig. 2.2a,c we present these results in the form of both amplitude $s(\omega)$ and phase $\phi(\omega) = \phi_3(\omega) - \phi_3^{Si}(\omega)$ spectra. Every data point in Fig. 2.2a,c was obtained by averaging over corresponding areas in images similar to those displayed in Fig. 2.1b.

## 2.4 Results

### 2.4.1 Near-field spectra of $SiO_2$

We first consider the near-field spectra of $SiO_2$. These spectra reveal a resonance centered at $\omega$ = 1128 $cm^{-1}$. The sharpness of the measured resonance, shown in Fig. 2.2a, establishes the notion of a surface phonon mode of amorphous $SiO_2$ in the near-field domain [17, 18, 19], as detailed below. The dominant spectral feature of $s(\omega)$ spectra for graphene on $SiO_2$ is similar to that for $SiO_2$ alone. However, the most surprising finding is that graphene strongly enhances the amplitude $s(\omega)$ in the 1110 – 1250 $cm^{-1}$ spectral region and also blue-shifts the peak frequency by about 10 $cm^{-1}$. We hypothesize that both effects are related to the high density of mobile carriers present in the graphene layer according to Raman measurements that we have performed on these samples. In order to verify this hypothesis, we monitored the variation of the resonance with gating voltage $V_g$ that enables controlled variation of the carrier density in graphene. Gating experiments were performed at $\omega = 1150$ $cm^{-1}$ where graphene enhances the scattering amplitude signal by 160% compared to $SiO_2$. At negative $V_g$ corresponding to higher hole density, the scattering amplitude is further enhanced and nearly four times that of $SiO_2$ at $V_g$ = -50 V. While positive $V_g$, which reduces the hole density, significantly suppresses the contrast between graphene and the oxide. The contrast is minimized at $V_g = (40 \pm 5)V$, which we assign to charge neutrality voltage $V_{CN}$. This estimate of $V_{CN}$ is in accord with the Raman probe of the carrier density in ungated graphene layers. In addition, graphene induces a steep increase of the near-field phase below 970 $cm^{-1}$ (Fig. 2.2c). We will show that the latter effect stems from direct

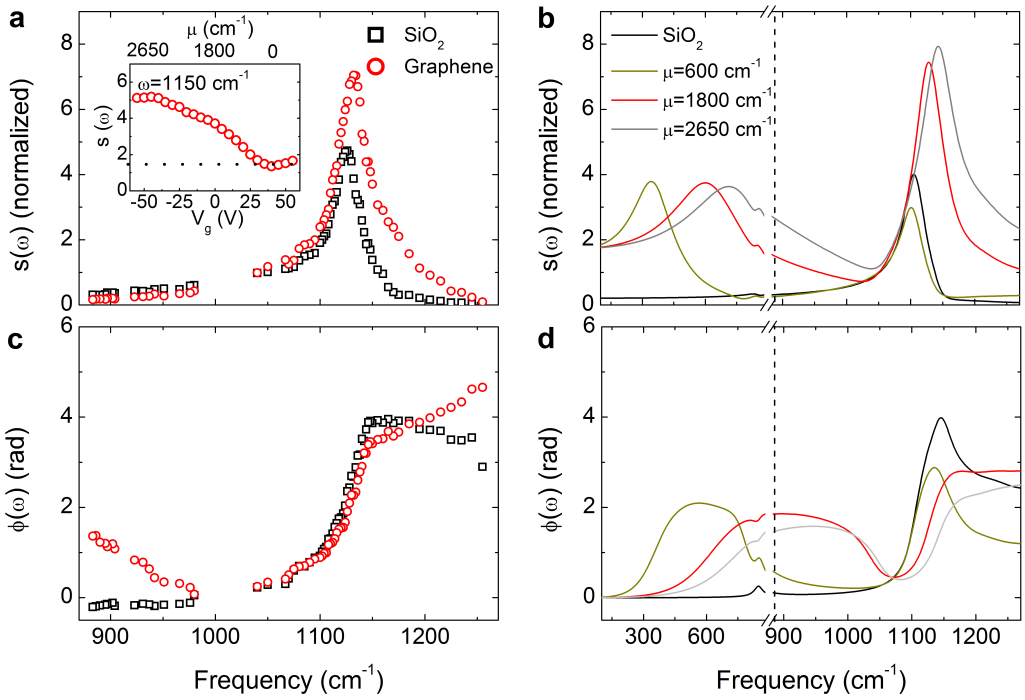


**Figure 2.2**: Spectra of the near-field amplitude $s(\omega)$ and phase $\phi(\omega)$. Panels (a),(c): experimental data extracted from images as in 2.1b for $SiO_2$ (black squares) and graphene on $SiO_2$ (red circles). The inset of Fig. 2.1a shows gating measurement result for the graphene near-field amplitude at $\omega = 1150$ cm$^{-1}$. The dotted line marks the value of gate-independent $SiO_2$ amplitude. Top axis of the inset marks the calculated chemical potential of graphene considering graphenes initial hole-doping ($\mu \sim 1800$ cm$^{-1}$) and the sample-wafer geometry. Panels (b),(d): dipole model spectra for $SiO_2$ (black) and graphene on $SiO_2$ (colors) for three different choices of the chemical potential $\mu = 600$, 1800, and 2500 cm$^{-1}$; (b) and (d) extend all model spectra to lower frequencies (left side of the dashed line) revealing direct near-field coupling of IR light to the Dirac plasmon of graphene.

interaction of ultra-localized IR light with the Dirac plasmon whereas $SiO_2$ resonance modifications originate from plasmon-phonon coupling at the graphene-$SiO_2$ interface.

The essential physics of the near-field interaction is that the tip, polarized by incident IR light, gives rise to evanescent fields with a wide range of in-plane momenta $q$. When the tip approaches a polar and/or conducting surface, the evanescent fields are altered which in turn affects the tip polarization. To quantify this interaction we introduce the reflection coefficient, $r_P(q,\omega)$, defined as the ratio of the amplitude of the $P$-polarized reflected field $E_r$ to that of the P-polarized incident field $E_i$. This frequency- and momentum-dependent response function completely describes the electrodynamics of the graphene-$SiO_2$ interface, not only in the near field, but also in the far field (see Supporting Information):

$$r_P(q,\omega) = \frac{\varepsilon_1 k_0 - \varepsilon_0 k_1 + (4\pi k_0 k_1 \sigma/\omega)}{\varepsilon_1 k_0 + \varepsilon_0 k_1 + (4\pi k_0 k_1 \sigma/\omega)} \tag{2.1}$$

In Equation 2.1, $\varepsilon_0$ is the dielectric constant of vacuum, $\varepsilon_1$ is the complex dielectric function of $SiO_2$, $k_j = \sqrt{\varepsilon_j(\omega/c)^2 - q^2}$ are the out-of-plane components of momenta, and $\sigma = \sigma(q,\omega)$ is the complex optical conductivity of graphene that obtained from the Radom Phase Approximation (RPA) method (see Supporting Information). $r_P(q,\omega)$ diverges at $q$ and $\omega$ values given by the dispersion of the two surface modes at the graphene/$SiO_2$ interface: the $SiO_2$ surface phonon and Dirac plasmon of graphene. A formal connection between $r_P(q,\omega)$ and the direct experimental observable of IR nanoscopy, $se^{i\phi}$, is worked out in Supporting Information (Eqs. S3) by modeling the apex of the tip as a point dipole. Here we only briefly comment on the essential aspects of the modeling procedure. An important parameter of our point-dipole model is the AFM tip radius $a$, which we have set at $a$ = 30 nm according to the specifications of our cantilevers. The tip radius determines the effective dipole polarizability $a^3$. Another significant parameter is the minimal dipole-sample distance $b$: the distance between the point dipole and the apex of the tip. Finally, we stress that the central result of the dipole-model analysis is that the $q$-dependent near-field coupling function has the weighting coefficient $q^2 exp(-2qz_d)$, where $z_d = b + \delta z(1 - cos\Omega t)$ is the coupling distance between the tip dipole and the sample surface (Eq. S2). The magnitude of $z_d$ is

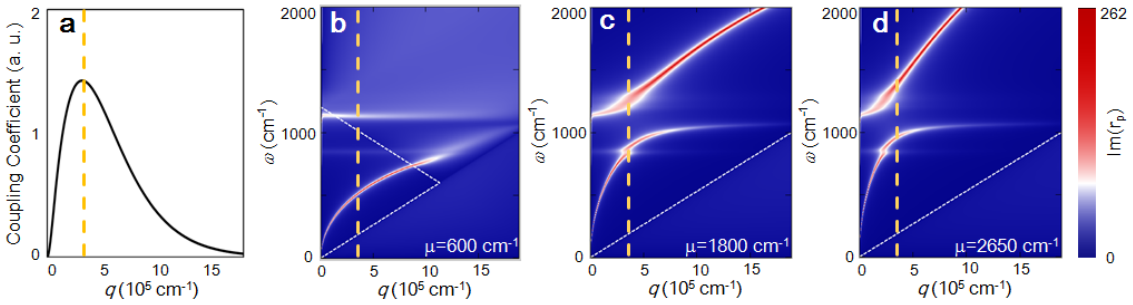


**Figure 2.3**: (a) The momentum dependence of time averaging near-field coupling coefficient $\langle q^2 exp(-2qz_d)\rangle_t$, which peaks at $q = 3.4 \times 10^5$ cm$^{-1}$ for our tip radius $a$ = 30 nm. (b)-(d) Imaginary part of the reflection coefficient $r_P(q,\omega)$ calculated using Eq. 2.1 with chemical potentials $\mu$= 600, 1800, and 2650 cm$^{-1}$, respectively and displayed in false color scale. Vertical yellow dashed lines in (a)–(d) mark the dominant $q$ for maximum near-field coupling. White dotted lines in (b)–(d) mark the boundaries of single-particle intra- and inter-band excitation continua of graphene; these two boundaries meet at ($q = k_F$, $\omega = \mu/\hbar$ ).

varying with time due to tip tapping; $\delta z = 40$ nm is the tapping amplitude. The plot of the time-averaged near-field coupling coefficient $\langle q^2 exp(-2qz_d)\rangle_t$ reveals a bell-shaped momentum dependence that peaks around $q = 1/a$ (Fig. 2.3a). Thus the dominant in-plane momenta contributing to near-field coupling are distributed around $q = 1/a$ (dashed line in Fig. 2.3a-d). For that reason, the $s(\omega)$ spectra show resonances if and only if the dispersion curve of a mode intersects the dashed line that marks the dominant near-field momentum. For a typical value of our tip radius, $a$ = 30 nm, the probing in-plane momentum exceeds that of the incident light at $\omega \sim 1000$ cm$^{-1}$ by about two orders of magnitude. These virtues of tip-enhanced near-field coupling enable the exploration of both the Dirac plasmon of graphene and plasmon-phonon coupling, which are fundamentally finite-momenta effects.

### 2.4.2 Dipole model

The dipole model of the near-field interaction [17, 18, 20], which we have adapted to the graphene-$SiO_2$ interface and augmented with the explicit account of the high-

momentum coupling, reproduces all aspects of the data (Figs. 2.2b,d). We first consider the near-field spectra of $SiO_2$. Comparing the results of dipole-model calculations with measurements, we find near quantitative agreement. Despite overall agreement between the data and modeling one witnesses minute discrepancies that may stem from two main factors. First, we used bulk optical constants of $SiO_2$ extracted from far-field ellipsometry measurements of our wafers in modeling the surface response (see Supporting Information). Second, the point-dipole model neglects the actual geometry of the tip that may introduce finite dipole or even higher multi-poles to the near-field interaction [19, 21, 22].

### 2.4.3 Graphene on $SIO_2$

We now proceed to describe the dipole-model results for graphene on $SiO_2$. In Figs. 2.2b,d we plot spectra of both amplitude and phase, displaying the evolution of the near-field response with the variation of the chemical potential $\mu$. For the specific choice of $\mu$ = 1800 cm$^{-1}$, we find that the model spectra reproduce the key characteristics of the data: enhancement of the resonance and its blue shift. The net result is that the Dirac plasmon of graphene radically modifies the $SiO_2$ surface phonon response, which is the experimental manifestation of the plasmon-phonon interaction at the graphene/$SiO_2$ interface. In order to map the dispersion of the plasmon we evaluated the divergence of $r_P(q,\omega)$ using Eq. 2.1 (Figs. 2.3c-d). The dispersion of the Dirac plasmon approximately follows the square-root $q$-dependence $\omega_P(q) \propto v\sqrt{k_F q}$ for $q$ values smaller than the Fermi wavevector $k_F$ [22]. Besides, the plasmon frequencies are also governed by the chemical potential (or carrier density $n$) in the graphene layer since $k_F = \sqrt{\pi n}$. It is customary to specify the carrier density with the chemical potential because the latter also determines the onset of interband transitions and cut-offs for intraband excitations (white dotted lines in Figs. 2.3b-d). Within the RPA approximation and considering constant scattering (by phonons or impurities) rate, the chemical potential alone defines the optical conductivity of graphene in the mid-IR region (see Supporting Information) [14, 23, 24]. In weakly doped graphene, the Dirac plasmon and the surface phonon of $SiO_2$ are well separated from each other (Fig. 2.3b). At moderate levels of carrier density, the plasmon approaches the surface phonon of $SiO_2$ leading to the familiar effects

of mode repulsion and hybridization (Fig. 2.3c). Increasing the carrier density further leads to drastic changes in the dispersion of both the plasmon and the surface phonon (Fig. 2.3d).

The dipole model predicts that the plasmon-phonon interaction and hybridization at the graphene-$SiO_2$ interface (Fig. 2.3b-d) can be readily observed by near-field nanoscopy. We focus on the chemical potential $\mu = 1800$ cm$^{-1}$: initial doping level of our graphene samples corresponding to the carrier density of $n \sim 2.9 \times 10^{12}$ cm$^{-1}$. The dipole model calculations carried out for $\mu = 1800$ cm$^{-1}$ show that the anti-crossing of the Dirac plasmon and the phonon not only causes the blue shift of the peak in $s(\omega)$ spectra but also increases the strength of the resonance (Fig. 2.2b). Both effects were observed by our experiment. Furthermore, the model predicts the systematic variation of the scattering amplitude with the chemical potential in the 1100 – 1250 cm$^{-1}$ range, which was observed by our gating experiments. Because graphene on $SiO_2$ is unintentionally doped, the enhancement of $s(\omega)$ is expected to show an non-monotonic variation with the gate voltage, and have the minimum near charge neutrality point. This is in accord with the data presented in the inset of Fig. 2.2a. In combination, near-field spectra in Fig. 2.2 and gating data at a selected probing frequency attest to the hybrid character of the resonance involving coupled plasmon-phonon oscillations that dominate the mid-IR response of the graphene-$SiO_2$ interface.

Yet another salient feature of the modeled spectra is a strong resonance close to the low-energy cut-off of our data (Figs. 2.2b,d). This resonance originates from the direct coupling between the near-field probe and the Dirac plasmon. The plasmon resonance is broadened due the rapid variation of its frequency in the momentum range near $q = 1/a$ (Fig. 2.3c). For a specific choice of the chemical potential $\mu$ = 1800 cm$^{-1}$ corresponding to the doping level of our samples, the resonance of Dirac plasmon in the amplitude spectrum $s(\omega)$ (Fig. 2.2b) appears at $\omega = 600$ cm$^{-1}$, which is beyond the range accessible by our lasers. Nevertheless, the corresponding feature in the phase spectra $\phi(\omega)$ (Fig. 2.2d) does extend into the experimentally accessible frequencies. We attribute the observed increase of the phase at low frequencies (Fig. 2.2c) to direct near-field coupling to the Dirac plasmon. This finding, along with the fingerprints of plasmon-phonon interaction, establishes graphene as a new medium supporting plas-

monic effects. Unlike noble metals: traditional materials supporting surface plasmons, graphene is inherently tunable by electric and magnetic fields, thus enabling functionalities not attainable with metal plasmonics.

## 2.5 Conclusions

The combination of high-momentum spectroscopy and nano-imaging demonstrated in our work sets the stage for studying many other properties of Dirac plasmons in graphene. Of special interest are effects pertaining to the real space confinement and propagation of plasmons in nano-structures/ribbons [25, 26]. A modification of the plasmon dispersion and/or ultra-fast modulation [27] of the Dirac plasmon (Fig. 2.3) can be conveniently carried out through back gating with a degree of control that is difficult to obtain within all-metal plasmonics. Turning to the high-$q$ spectroscopy aspects of tip-induced optical interaction, we want to point out that a much broader range of $q$ may be interrogated using sharper (sub-10 nm) tips and also ultra-sharp (a down to 1 nm) tips based on carbon nano-tubes [28]. Such a further expansion of the momentum space accessible by IR nanoscopy, combined with the improved spatial resolution, are especially appealing in the context of studying collective modes in the vicinity of the single-particle excitation continuum, and manipulating light in graphene-based nanostructures or transformation optics elements.

## 2.6 Supporting Information

### 2.6.1 Experimental

AFM images were collected simultaneously with the infrared images shown in Fig. 2.1b. In Fig. 2.4, we show two separate parts of a typical AFM image together with two height profiles. The profile across the $SiO_2$/graphene boundary shows about 1 nm thickness which is typical for exfoliated monolayer graphene on $SiO_2$/Si substrate. The profile across the Si/$SiO_2$ boundary shows that the 300 nm thick $SiO_2$ layer is totally etched away in the left part where we can get access to the silicon reference.

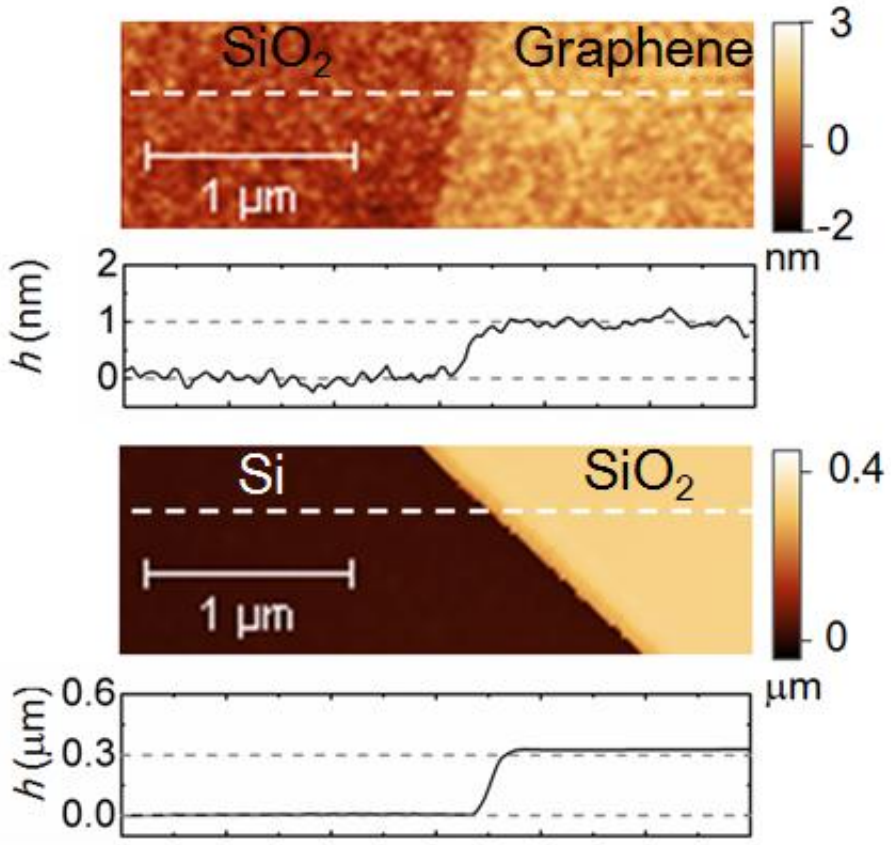


**Figure 2.4**: AFM topography in the vicinity of the graphene-$SiO_2$ and Si-$SiO_2$ boundaries. We also show topographical height profiles along the dashed lines in the images.

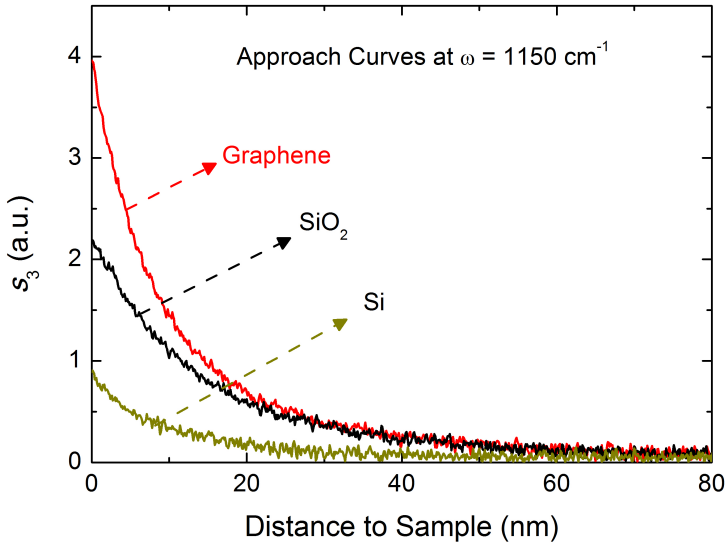


**Figure 2.5**: Typical infrared approach curves at $\omega = 1150\,\mathrm{cm}^{-1}$ at three different sample positions attest to the genuine near-field signal recorded by our apparatus.

The approach curves shown in Fig. 2.5 measure the infrared amplitude as a function of the separation between the oscillating tip apex and the sample surface. The observed sharp decrease within a 20 nm scale verifies that the experimental parameters are set to record the genuine near-field interaction [29].

Raman spectroscopy was used to choose monolayer graphene samples with identical unintentional doping level. In Fig. 2.6, we show Raman spectra for two typical graphene samples studied in this work. The intensity ratios between the 2D mode and G mode are larger than 2 for both sample 1 and 2 verifying that both samples are monolayer graphene. The Raman shift for the *G* mode of both samples is close to $1587.6\,\mathrm{cm}^{-1}$ corresponding to charge density of $(3\pm1)\times10^{12}\,\mathrm{cm}^{-1}$ according to refs. [30, 31]. Considering the $SiO_2$ layer being 300 nm thick, the charge neutral point from both samples are close to $(40\pm10)$ V and both samples have identical doping in accord with chemical potential $\mu = (1800\times200)\,\mathrm{cm}^{-1}$.

In Fig. 2.7, we plot the optical constants of $SiO_2$ used in our modeling that were modified from far-field ellipsometry result of our $SiO_2$/Si wafers. We used Lorentz oscillators $\varepsilon(\omega) = \varepsilon_\infty + \sum_i f_i \frac{\omega_i\Gamma_i}{{\omega_i}^2-\omega^2-i\omega\Gamma_i}$ to fit the optical constants. Here $\varepsilon_\infty$ =1.8, and

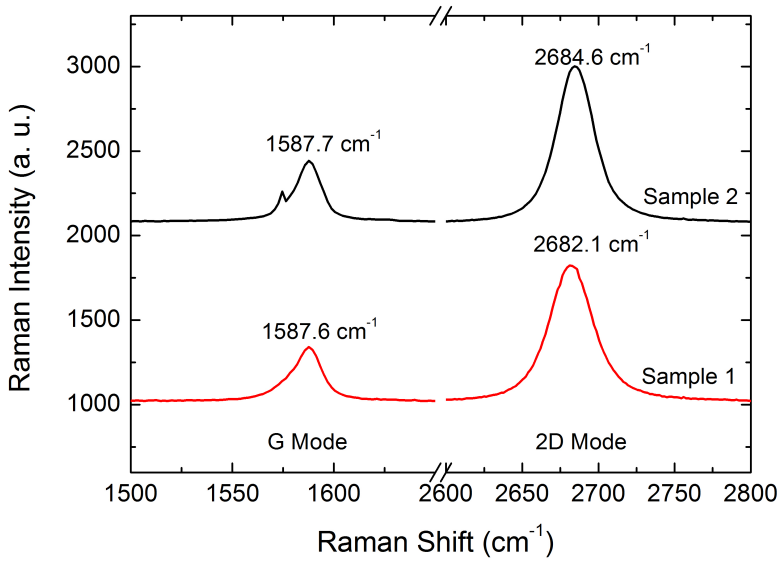


**Figure 2.6**: Raman spectra (using 514.5 nm laser) for two typical graphene samples chosen in this work.

other parameters are given in Table2.1.

### 2.6.2 Theoretical model and interpretation

### 2.6.3 Point-dipole approximation for the s-SNOM

The experimental technique used in this work is commonly referred to as scattering scanning near-field optical microscopy (s-SNOM) [19, 20]. Our theoretical analysis follows the formalism developed previously for multilayer systems [32] with some mod-

**Table 2.1**: Detailed parameters for Lorentz oscillators used to fit the optical constants of $SiO_2$.

| | **1** | **2** | **3** | **4** |
|---|---|---|---|---|
| $f_i$ | 0.5 | 15 | 0.2 | 0.2 |
| $\omega_i$ | 845 | 1072 | 1205 | 1250 |
| $\Gamma_i$ | 50 | 30 | 77 | 115 |

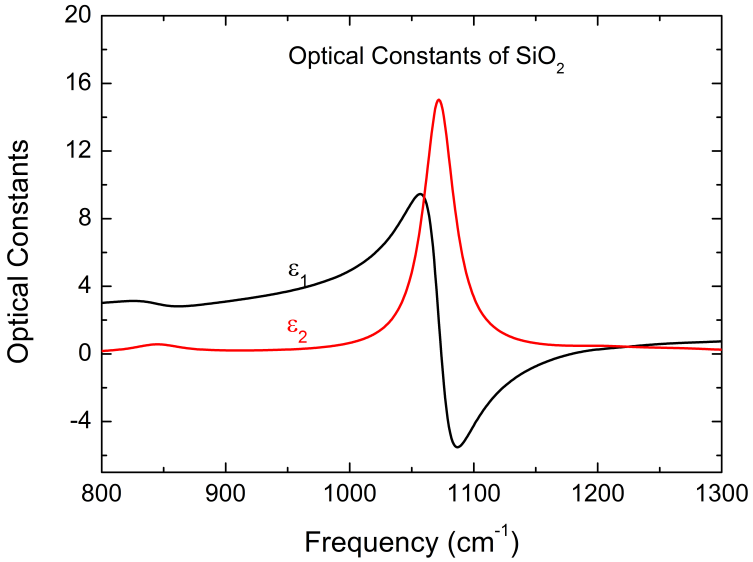


**Figure 2.7**: Real and imaginary part of $SiO_2$ permittivity obtained from ellipsometry measurement.

ifications needed to account for the two-dimensional nature of graphene.

The measured s-SNOM signal represents the electromagnetic field backscattered by the probe and the scanned sample. In the tapping mode, the distance $z$ between the sample and the tip apex undergoes harmonic oscillations with a typical tapping amplitude $\Delta z$ = 40 nm. As a result, the complex amplitude $s(\omega,t)$ of the backscattered field varies periodically with the tapping frequency $\Omega$. The experimental observables are the absolute values $s_n(\omega)$ and phases $\phi_n(\omega)$ of tapping harmonics. Extracting $s_n$ and $\phi_n$ from $s(\omega,t)$ is termed demodulation. The data presented in the main text was demodulated at order $n = 3$. The demodulation suppresses the unwanted background and isolates the part of the signal scattered by the tip of the probe (a region of size: $\Delta z$). This enables one to study the near-field interaction between the probe and the sample, which modifies the dipole moment $\mathbf{p}(z)e^{-\omega t}$ induced on the probe by the incident light.

Previous s-SNOM studies demonstrated that $\mathbf{p}$ can be computed analytically if the tip is approximated by a spheroid [22, 29, 33], a small sphere [29, 34, 35, 36, 37], a finite dipole [21, 19], or a point dipole [17, 20, 38]. Adopting the last model, we characterize the tip by two adjustable parameters: polarizability $a^3$ where $a$ is of the

order of its radius of curvature and the distance $b$ between the effective dipole and the lowest point of the tip. The distance between the dipole and the interface is therefore

$$z_d(t) = b + z(t) = b + \Delta z(1 - \cos\Omega t) \tag{2.2}$$

We further assumed that the tip responds only to the vertical $(z)$ component of the electric field because the actual tip has the highest polarizability along its longest dimension, like an antenna. Under this assumption, only the $P$-polarized component of the incident wave contributed to the signal. Similarly, only the reflection coefficient $r_P(q,\omega)$ for the $P$-polarization is important for computing the tip-sample coupling function $G$:

$$G(z_d,\omega) = \int_0^\infty dq\, q^2 e^{-2qz_d} r_P(q,\omega) \tag{2.3}$$

The weighting coefficient $q^2 e^{-2qz_d}$ inside the integral has a maximum centered at $q = 1/z_d : 1/(b+\Delta z)$, see Fig. 2.3(a) of the main text. It defines a range of momenta where the s-SNOM can probe the surface excitation spectrum of the system most effectively. In our experiments, this range corresponds to $q \sim 3.4\times 10^5$ cm$^{-1} \gg \sqrt{\varepsilon_0}\omega/c$.

The final result for the demodulated signal is (cf. Ref. 4)

$$s_n e^{i\phi_n} \propto \sin^2\theta \int_0^{2\pi} \frac{e^{in\phi}\, d\phi}{1 - G(b+\Delta z(1-\cos\phi),\, \omega)a^3} \tag{2.4}$$

As a first application of these formulas, consider a bulk $SiO_2$ sample. The reflection coefficients are given by the usual Fresnel formulas

$$r_P(q,\omega) = \frac{\varepsilon_1 k_0 - \varepsilon_0 k_1}{\varepsilon_1 k_0 + \varepsilon_0 k_1} \tag{2.5}$$

where subscripts $j = 0$ and 1 refer to vacuum and $SiO_2$, respectively, $\varepsilon_j$ are the dielectric functions (e.g., $\varepsilon_0 = 0$), and $k_j$ are the $z$-components of the momenta:

$$k_j = \sqrt{\varepsilon_j \frac{\omega^2}{c^2} - q^2}, \qquad \Im k_j \geq 0 \tag{2.6}$$

at $q \gg \sqrt{\varepsilon_0}\omega/c$, where, the reflection coefficient $r_P$ becomes $q$-independent. In previous literature [39, 40, 21] this $q$-independent value was denoted by $\beta(\omega)$ :

$$r_P \approx \beta(\omega) \equiv \frac{\varepsilon_1 - \varepsilon_0}{\varepsilon_1 + \varepsilon_0} = 1 - \frac{\varepsilon_0}{\kappa(\omega)} \tag{2.7}$$

$$\kappa(\omega) = \frac{\varepsilon_0 + \varepsilon_1}{2} \tag{2.8}$$

The main spectroscopic feature of $|\beta(\omega)|$ is a maximum at the surface phonon frequency, which is approximately 1140 cm$^{-1}$ in our sample. Function $|G|$ mirrors the behavior of $|\beta(\omega)|$ because for $q$-independent $r_P$ Eq. 2.3 yields $G(z_d,\omega)=\beta(\omega)a^3/4z^3{}_d$.

The 3rd harmonic component $s_3e^{i\phi_3}$ of the s-SNOM signal, needed for comparison with the experiment, is obtained from $G$ via the nonlinear operation of demodulation, Eq. 2.4. Using reasonable values $a$ = 30 nm and $b=0.7a$ of the two adjustable parameters, we achieve a good agreement between this simple model and the measurements, see Fig. 2.2 of the main text. Our results for $SiO_2$ are also in a good agreement with a recent s-SNOM study [39] of $SiO_2$ (both crystalline and amorphous), in which the main maxima in $s_n$ were found at 1120 – 1130 cm$^{-1}$ (In crystalline $SiO_2$ additional small maxima have also been reported.).

### 2.6.4 Application to the graphene-$SiO_2$ interface

When we apply the outlined formalism to the case where the surface of $SiO_2$ is covered with graphene. Consider the in-plane momenta satisfy the strong inequality $\omega/c \gg q \gg \omega/v$, where $v \approx c/300$ is the Fermi velocity of graphene. Because of that, the expression for $r_P(q,\omega)$ can be brought to the form analogous to Eq. 2.7:

$$r_P(q,\omega)=1-\frac{\varepsilon_0}{\kappa(\omega)\varepsilon(q,\omega)} \tag{2.9}$$

Where 2D dielectric function $\varepsilon(q,\omega)$ of graphene [16-18] is given by

$$\varepsilon(q,\omega)=1-\frac{2e^2}{\kappa(\omega)}\frac{q}{\hbar\omega}\left[\frac{|\mu|}{\hbar\varsigma}-\frac{1}{4}\ln\left(\frac{2|\mu|+\hbar\varsigma}{2|\mu|-\hbar\varsigma}\right)\right], \qquad \varsigma\equiv\omega+i\gamma \tag{2.10}$$

$\mu$ is the chemical potential of graphene, and $\gamma>0$ is the phenomenological scattering rate of quasiparticles. In our calculation, we apply $\gamma\sim 0.09\omega$ to mimic experimental optical conductivity of graphene in Ref. [14].

The $P$-polarized (i.e. TM) collective mode spectra of the system can be extracted from this equations as follows. The first method is to look for poles of $r_P$. This leads us to the equation

$$\varepsilon(q,\omega_P(q))=0 \tag{2.11}$$

which is a familiar equation for the plasmon. Under the earlier assumption $\omega \gg vq$, it has a solution of the form [41, 42, 6, 43, 44, 45, 46] $\omega_P(q)\approx v\sqrt{2\alpha(\omega_P)k_Fq}$,

where $\alpha(\omega) = e^2/\hbar v \kappa(\omega)$ is a dimensionless measure of the Coulomb interaction strength. For constant $\alpha$, Eq. S26 gives the usual $\sqrt{q}$-dispersion of a 2D plasmon. A frequency-dependent dielectric function of the substrate causes $\alpha$ to become a complex-valued function of $\omega$. This introduces shift and broadening of the plasmon mode. This effect has been studied experimentally in Refs. [41, 42, 47, 6] and theoretically in Ref. [21] for the case of graphene on SiC.

Equation S25 has another solution, which becomes more apparent if this equation is rewritten as

$$\kappa(\omega) = \frac{2e^2 q}{\hbar\omega}\left[\frac{|\mu|}{\hbar\varsigma} - \frac{1}{4}\ln\left(\frac{2|\mu| + \hbar\varsigma}{2|\mu| - \hbar\varsigma}\right)\right] \tag{2.12}$$

At $q = 0$ and $\omega \neq 0$ , it gives $\kappa(\omega) = 0$ , which corresponds to the pole of $r_P$ in the absence of graphene, cf. Eq. 2.7. Therefore, this solution represents the surface phonon. By continuity, it gives rise to the entire branch of dispersion SP coupled with plasmon at finite $q$. Therefore, our formalism captures both types of collective modes as well as their interaction.

Solving Eq. 2.12 is not the most practical way to extract the desired mode spectra. Instead, we follow another common procedure and obtain them from the condition of maximum dissipation, which is realized at the maxima of $\Im r_P$. The spectra can be conveniently visualized by a pseudocolor plot of $\Im r_P$ as a function of $q$ and $\omega$. This plot is presented in Fig. 2.3 of the main text where one can clearly see two dispersion curves.

Finally, substituting Eq. 2.9 into Eqs. 2.3 and 2.4 and doing numerical quadrature, we comptute the near field coupling $G$ and the demodulated s-SNOM signal for the point-dipole model of the tip. We use the same parameter $a$ and $b$ as in the previous section. As shown in Fig. 2.2 of the main text, this time function $s_3(\omega)$ has two maxima: one near the surface phonon resonance and the other near the plasmon resonance. The latter shows up as a rather broad feature because the integral in Eq. 2.3 has contribution not from a single $q$ but from a range of momenta. The strength and position of these spectroscopic features depend on the chemical potential $\mu$. Therefore, they can be used to estimate $\mu$ in the experiment.

## 2.7 Acknowledgements

The author would like to thank the co-authors of this publication for allowing its usage in this dissertation:

Z. Fei, G. O. Andreev, W. Bao, L. M. Zhang, Z. Zhao, G. Dominguez, M. Thiemens, M. M. Fogler, C. N. Lau, F. Keilmann, and D. N. Basov. ”Dirac plasmons at the graphene-SiO2 interface”. (submitted), 2011.

# Bibliography


[1] H. A. Atwater. *Sci. Am.*, 296:56–63, 2008.

[2] P. R. West. and S. Lshii, G. V. Naik, N. K. Emani, V. M. Shalaev, and A. Boltasseva. *Laser & Photon Rev.*, pages 1–13, 2010.

[3] J. A. Schuller, E. S. Barnard, W. Cai, Y. C.Jun, J. S. White, and M. L.Brongersma. *Nature Mater.*, 9:193–204, 2010.

[4] M. I. Stockman. *Phys. Today*, 64:39–44, 2011.

[5] F. Bonaccorso, Z. Sun, T. Hasan, and A. C. Ferrari. *Nature Photon*, 4:611–622, 2011.

[6] K. W.-K.Shung. *Phys. Rev. B*, 34:979–993, 1986.

[7] Y. Liu and R. F. Willis. *Phys. Rev. B*, 81:081406(R), 2010.

[8] R. J. Koch, T. Seyller, and J. A. Schaefer. *Phys. Rev. B*, 82:201413, 2010.

[9] F. H. L. Koppens, D. E. Chang, and F. J. Garcia de Abajo. *ArXiv*, page 1104.2068, 2011.

[10] M. Jablan, H. Buljan, and M. Soljacic. *Phys. Rev. B*, 80:245435, 2009.

[11] A. Vakil and N. Engheta. *Science*, 332:1291–1294, 2011.

[12] A. Yu. Nikitin, F. Guinea, F. J. Garcia-Vidal, and L. Martin-Moreno. *ArXiv*, page 1104.3558, 2011.

[13] D. N. Basov and T. Timusk. *Rev. Mod. Phys.*, 77(2):721–779, 2005.

[14] Z. Q. Li, E. A. Henriksen, Z. Jiang, Z. Hao, M. C.Martin, P. Kim, H. L. Stormer, and D. N. Basov. *Nature Phys.*, 4:532–535, 2008.

[15] L. Novotny and B. Hecht. *Principles of nano-optics*. Cambridge University Press, 2006.

[16] N. Ocelic, A. Huber, and R. Hillenbrand. *Appl. Phys. Lett.*, 89:101124, 2006.

[17] J. Aizpurua, T. Taubner, F. J. G. Abajo, M. Brehm, and R. Hillenbrand. *Opt. Express*, 16:1529–1545, 2008.

[18] R. Hillenbrand, R. Taubner, and F. Keilmann. *Nature*, 418:159–162, 2002.

[19] S. Amarie and F. Keilmann. *Phys. Rev. B*, 83:045404, 2011.

[20] R. Hillenbrand and F. Keilmann. *Phys. Rev. Lett.*, 85:3029–3032, 2000.

[21] A. Cvitkovic, N. Ocelic, and R. Hillenbrand. *Opt. Express*, 15:8550–8565, 2007.

[22] J. A. Porto, P. Johansson, S. P. Apell, and T. Lo'pez-Ros. *Phys. Rev. B*, 67:085409, 2003.

[23] F. Wang, Y. Zhang, C. Tian, C. Girit, A. Zettl, M. Crommie, and Y. R. Shen. *Science*, 320:206–209, 2008.

[24] T. Stauber, N. M. R. Peres, and A. H. Castro Neto. *Phys. Rev. B*, 78:085418, 2008.

[25] M. Y. Han, B. Ozyilmaz, Y. Zhang, and P. Kim. *Phys. Rev. Lett.*, 98:206805, 2007.

[26] X. Li, X. Wang, L. Zhang, S. Lee, and H. Dai. *Science*, 319:1229–1231, 2008.

[27] F. Xia, T. Mueller, Y.-M. Liin, A. V. Garcia, and P. Avouris. *Nature Nano*, 4:839–843, 2009.

[28] R. Hillenbrand, F. Keilmann, P. Hanarp, D. S. Sutherland, and J. d Aizpurua. *J. Appl. Phys. Lett.*, 83:368–370, 2003.

[29] J. Renger, S. Grafström, L. M. Eng, and R. Hillenbrand. *Phys. Rev. B*, 71:075410, 2005.

[30] S. Pisana, M. Lazzeri, C. Casirachi, K. S. Novoselov, A. K. Geim, A. C. Ferrari, and F. Mauri. *Nature mater.*, 6:198–201, 2007.

[31] J. Yan, Y. Zhang, P. Kim, and A. Pinczuk. *Phys. Rev. Lett.*, 98:166802, 2007.

[32] Z. H. Kim and Leone S. R. *J. Phys. Chem. B*, 110:19804–19809, 2006.

[33] R. Esteban, R. Vogelgesang, and K. Kern. *Opt. Express*, 17:2518–2529, 2009.

[34] R. W. Rendell and D. J. Scalapino. *Phys. Rev. B*, 24:3276–3294, 1981.

[35] P. K. Aravind and H. Metiu. *J. Phys. Chem.*, 86:5076–5084, 1982.

[36] P. K. Aravind and H. Metiu. *Surf. Sci.*, 124:506–528, 1983.

[37] Sukhov S. V. *Ultramicroscopy*, 101:111–122, 2004.

[38] T. Taubner, F. Keilmann, and R. Hillenbrand. *Nano Lett.*, 4:1669–1672, 2004.

[39] F. Keilmann and R. Hillenbrand. *Phil. Trans. Roy. Soc. London, Ser. A*, 362:787–805, 2004.

[40] F. Keilmann and R. Hillenbrand. Near-field nanoscopy by elastic light scattering from a tip. In *Nano-optics and near-field optical microscopy*. Artech House, Norwood, 2009, 2009.

[41] B. Wunsch, T. Stauber, F. Sols, and F. Guinea. Dynamical polarization of graphene at finite doping. *New J. Phys.*, 8:318, 2006.

[42] E. H. Hwang and S. Das Sarma. *Phys. Rev. B*, 75:205418, 2007.

[43] K. W.-K.Shung. *Phys. Rev. B*, 34:1264–1272, 1986.

[44] O. Vafek. *Phys. Rev. Lett.*, 97:266406, 2006.

[45] S. Gangadharaiah, A. M. Farid, and E. G. Mishchenko. *Phys. Rev. Lett.*, 100:166802, 2008.

[46] A. Hill, S. A. Mikhailov, and K. Ziegler. *Phys. Rev. Lett.*, 87:27005, 2009.

[47] A. H. Castro Neto, F. Guinea, N. M. R. Peres, K. S. Novoselov, and A. K. Geim. *Rev. Mod. Phys.*, 81:109–162, 2009.

# 3 Infrared Nanooptics of Ultrathin Materials

## 3.1 Abstract

We demonstrate an infrared nanooptics approach capable of material characterization for 3D volumes smaller than $< 10 \times 10 \times 1nm^3$ using the technique of infrared scattering Scanning Near-field Optical Microscopy (sSNOM). We present the first nanoscale infrared images of an ultrathin conductor: suspended single layer Graphene, and an ultrathin amorphous insulator: $\leq 2nm$ thick $SiO_2$. For both materials, we see strong image contrasts which allow a spatial resolution of $\leq 10 \times 10nm$ to be achieved. For Graphene we attribute the origin of the contrast to the presence of nanoscale carrier density inhomogenieties in the suspended Graphene layer. In the case of $SiO_2$, the contrast stems from surface phonon excitation. This conclusion is also supported by the thickness dependence observed in broadband nanospectra obtained on $SiO_2$ layers with thicknesses ranging from $2 - 300nm$. Our results on single layer suspended Graphene and ultrathin $SiO_2$ confirm that the evanescent waves produced in our sSNOM provide in-plane excitation with light momenta as high as $|q| > \frac{300}{\lambda}$.

## 3.2 Introduction

The diffraction limit imposes significant constraints on the spatial resolution achievable with conventional far field optical techniques, especially when the latter are employed to imaging and spectroscopy over a broad band of frequencies. Broadband

infrared nanooptics is highly desirable since it would allow nanoscale characterization of materials via vibrational modes or electronic excitation [1]. The ability to probe both material properties at the nanoscale is possible with the method of sSNOM. In this technique, light incident on a sharp metallic tip creates highly confined electric fields directly outside of the tip apex via the optical lightning rod effect [1]. The nanoscale volume of the apex (typical radius $a < 30nm$) essentially acts as a nanoantenna source of large momentum (high spatial frequency) ($|q| \approx \frac{1}{a} >> \frac{\omega}{c}$) evanescent fields for any wavelength satisfying $\lambda >> a$. The evanescent fields reflect off the sample surface creating an electrostatic image effect for the polarized tip[2]. By measuring the portion of the nanoantenna's far field radiation due to the charge concentrated at the tip's apex, it is possible to gain information about the nanoscale optical properties of the sample (3.1right)[3]. This approach has been used in such applications as 20nm resolved imaging of a tobacco mosaic virus, stress mapping of a nanocrack, imaging of the metal to insulator transition in $VO_2$, or nanoscale polymer identification [4, 5, 6, 7]. While the aforementioned studies established sub-20nm in-plane sensitivity as a benchmark for infrared microscopy, we are aware of only a few experiments which have investigated the sensitivity of sSNOM in the out-of-plane direction, such as: the subsurface detection of $> 40nm$ deep gold islands [8] or resonant substrate enhanced characterization of a $10nm$ thick PMMA layer [2]. Here, we present the first application of broadband imaging and spectroscopy to even thinner materials: suspended single atomic layers of Graphene and $2-300nm$ thin layers of $SiO_2$ on Silicon. We note that the material contrasts we observed stem from the free carrier, electronic response of Graphene and in the case of $SiO_2$, vibrational modes, demonstrating that we are indeed sensitive to both types of material characterization.

## 3.3 Experimental

The sSNOM (Neaspec) used in our experiments is a modified Atomic Force Microscope (AFM) with a built in parabolic focusing mirror and a pseudoheterodyne interferometer. The AFM operation is done in tapping mode which also serves the dual

[1] By electronic excitations we mean features relevant to IR spectroscopy such as the width of a Drude peak or a plasmon excitation

purpose of modulating the tip-sample near field interaction. A bank of tunable External Cavity-Quantum Cascade Lasers (EC-QCLs) (Daylight Solutions) and two $CO_2$ lasers (Access Lasers), with center frequencies ranging from $800-2200cm^{-1}$, serve to provide intense infrared light focused onto a metallized tip by a parabolic mirror. The same parabola also simultaneously collects the tip's scattered light. The scattered light contains both unwanted background fields and the desired near fields: $E_{scat} = E_{bg} + E_{nf}$. Since the near fields are highly nonlinear with distance, they can be written as a sum of harmonics at the tapping frequency: $E_{nf} = \Sigma_{n=1}^{\infty} S_n e^{i\phi_n} Cos(n\Omega t)$ whereas the background fields are largely independent of the tapping frequency. The resultant parallel beam is sent back to reflect from the broadband ZnSe beam splitter to a Mercury Cadmium Telluride infrared detector 3.1. There it is combined with a reference field which has traveled along the other path of the interferometer, reflecting off an oscillating mirror in the process. We write this field as $E_{ref} \propto \Sigma_{-\infty}^{\infty} i^m J_m(\gamma) e^{mMt}$ where $J_m$ are Bessel functions of the first kind at the $m^{th}$ harmonic of the mirror oscillation frequency $M$ and $\gamma$ is the modulation depth, in radians. Under this "pseudoheterodyne" detection scheme, the voltage at the detector, $V \propto \left|E_{bg} + E_{nf} + E_{ref}\right|^2$, contains the term $E_{ref} E_{nf} Cos(\phi_{nf} + \phi_{ref})$ where $\phi_{nf}$ and $\phi_{ref}$ are the phase of the near and reference fields respectively. By measuring this term selectively, the near field can be "assymetrically" amplified by over 4 orders of magnitude due to the large amplitude of $E_{ref}$[9]. To extract just this term from the voltage, the additional modulation on $E_{nf}$ by $E_{ref}$ is utilized to suppress the parasitic crossterm: $E_{bg} E_{nf} Cos(\phi_{nf} + \phi_{bg})$. The key is that $E_{bg}$ is largely unmodulated by the tip motion or at best modulated at $\Omega$. Thus by demodulating $V$ at $n\Omega + M$ and $n\Omega + 2M$ frequencies with $n \geq 2$ we can, after some algebra, arrive at the background near field amplitude and phase harmonics: $S_n$ and $\Phi_n$. For the purposes of this publication we limit the discussion to $n = 2$ and $n = 3$ harmonics for all the data presented.

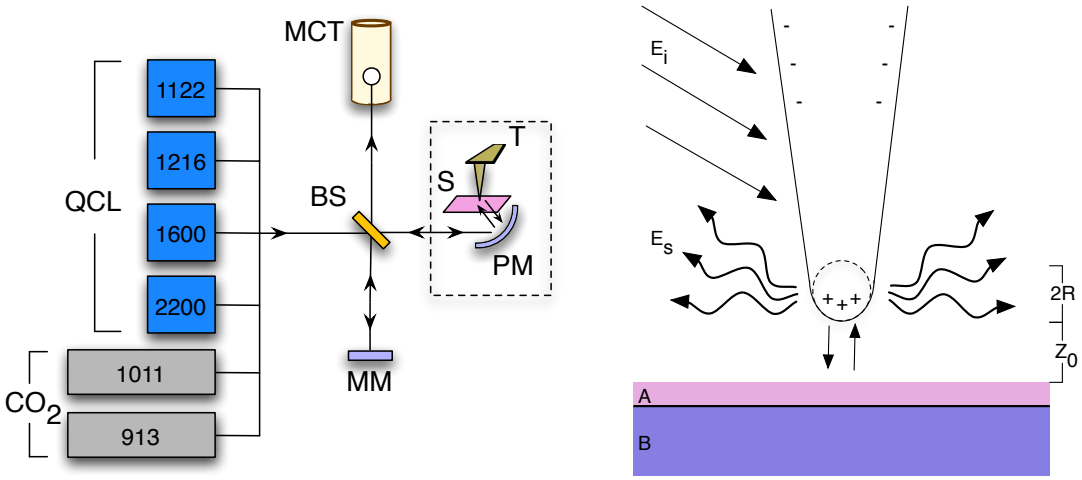


**Figure 3.1**: Left: Optical path of the broadband sSNOM instrumentation. IR light (black arrows) is generated by an array of lasers comprised of 4 EC-QCLs and 2 $CO_2$ lasers (left) with center frequency indicated, in $cm^{-1}$. The light enters an asymmetric interferometer composed of the elements: BS = ZnSe Beam Splitter, MM = Oscillating Mirror, MCT = Mercury Cadmium Telluride detector, PM = Parabolic Mirror,T = Metallized Tip, S = Sample. Right: A detailed view of the dashed rectangle area in the left panel. Incident fields, $E_i$, polarize the end of a tip of radius $a$ and distance $z_0$ from the sample. The sample is composed of a thin layer A on substrate B. Near fields produced by the tip reflect off the sample contributing to the overall scattered field by the tip, $E_s$. The PM collects the scattered field allowing the parallel beam to combine at the MCT with amplifying reference beam from the MM leg.

## 3.4 Results and discussion

### 3.4.1 Nanoimaging of a Freestanding Conducting Monolayer

In 3.2 we present nanoscale IR images of a single Graphene layer, a portion of which is freestanding over a trench $2\mu m$ wide and 300nm deep (top left panel). Raman spectroscopy, AFM, and optical microscopy were used to confirm that this is only a single atomic layer of Graphene. In 3.2a we present amplitude $S_3$ and phase $\Phi_3$ IR images at frequency $\omega = 1250cm^{-1}$, normalized to the equivalent signals from Silicon. We emphasize this frequency because here the adjacent supported Graphene on Substrate (GOS) is highly suppressed by the *LO* phonon mode of the $SiO_2$ substrate. Because of

this effect the near field signal of suspended Graphene is made remarkably stronger than the supported Graphene at this frequency. This is also evident from normalized line profiles of $S_3$ ( 3.2c) relative to Silicon, the observed near field signals for both SG and GOS

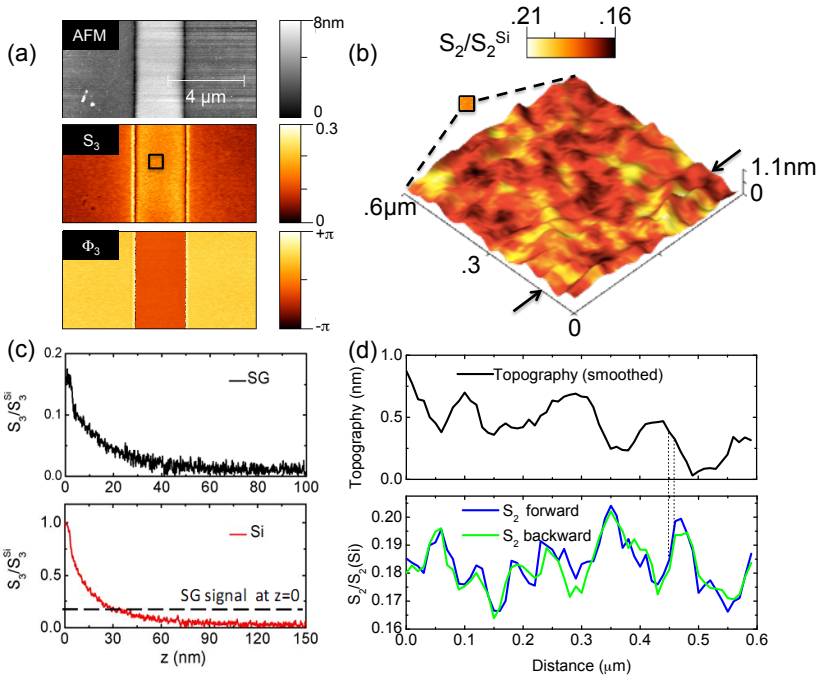


**Figure 3.2**: (a)Simultaneously obtained images of topography (top panel), normalized (to Silicon) 3rd harmonic of scattering amplitude (middle panel) and phase (bottom panel) at $\omega = 1250cm^{-1}$. (b) Zoomed in forward scan direction $S_2$ image at $\omega = 1192cm^{-1}$ of the boxed region in (a) (c) The $S_3$ approach curves described in the text for both suspended graphene and silicon at $\omega = 1250cm^{-1}$. The black dashed line denotes the suspended graphene signal when the tip is in contact with the sample. (d) profiles of AFM topography (top) and $S_2$ obtained along the path connecting the black arrows in (c). The $S_2$ profiles are for the forward and backward scanning direction.

are quite small, at .18 and .08. Nevertheless our technique attains a signal to noise ratio more than sufficient to directly observe the optical response of Suspended Graphene. We demonstrate this claim by comparing $S_3$ approach curves of Suspended Graphene to Silicon ( 3.2c) performed on the same overall sample, with the identical tip and at the same frequency. Approach curves provide an effective measure of the near field signal's decay with tip/sample distance. A true near field signal displays a character-

istically near-exponential decay with increasing tip-sample distance, with decay length proportional to the tip radius, $a \approx 25nm$. This is directly observed in the third harmonic of our measured near field amplitude. Both Silicon and SG approach curves show a very sharp drop off, reaching $\frac{1}{e}$ of their maxima by $z \approx 18nm$. We can also estimate the total amount of background signal by checking the $S_3$ value at large distances in the approach curve, i.e. $z = 100nm$. Here the value of $S_3$ is $< 5\%$ of that at the $z = 0nm$ "in-contact" distance where imaging and AFM measurements are performed. At the 2nd harmonic we achieve similar performance, with approximately 15% background. These observations indicate that the observed near field signal at harmonics $n = 2,3$ is in large part due to direct interaction with the sample and not anharmonic mechanical oscillations or other details of the experimental conditions.

Suspended Graphene is detectable at other frequencies as well, as shown in the high resolution $\omega = 1180cm^{-1}$ $S_2$ image (3.2b) of the boxed region in (3.2a).This 3D image is a projection of the topography obtained by AFM with a color overlay indicating the local IR signal $S_2$. From this combined view, we can clearly distinguish areas of large near field signal which do not correlate with any topographical features such the surface roughness (on the order of $1nm$). To further illustrate this point, we show representative line profiles along the path connecting the two black arrows in (3.2b) of Topography and $S_2$ acquired in the Forward and Backward scanning directions. By comparing variations in the Topography profile (black) to the $S_2$ profiles (blue) we do not see any obvious correlations. The excellent $\approx 10nm$ scan to scan agreement between the forward and backward $S_2$ profiles (dashed lines 3.2d) also indicates that any sort of random noise, such as laser power fluctuations, cannot be the main origin of the spatial variation in our signals. The sharpness of the features is thus a measure of the lateral optical resolution of our technique. One such feature is the sharp edge indicated by the two dashed lines spaced $10nm$ apart. The reproducibility of this edge, as well as all others, in both the forward and backward scans, demonstrates the observation of a real, $< 10nm$ sharp optical feature within the suspended Graphene.

We postulate that the origin of the observed optical variation lies in an inherent spatial inhomogeneity in the Suspended Graphene carrier density or equivalently the Fermi energy $E_f$. This conclusion is qualitatively consistent with previous experiments

and theoretical predictions [10] [11]. Our detailed theoretical calculations (see Supplemental Material) allow us to estimate an upper bound on the range of spatial variation in $E_f$ and $\Gamma$ needed to produce the observed contrasts in $S_2$. We find this to be approximately $E_f \approx 650 \pm 50 cm^{-1}$ and $\Gamma \approx 100 cm^{-1} \pm 50 cm^{-1}$. Our results are close to the upper bound on carrier density estimated previously using Raman spectroscopy[12]. We also note that the Fermi Energy extracted from our data is much smaller than the supported Graphene portion of the same sample, where $E_f \approx 1300 cm^{-1}$.

These measurements of Suspended Graphene, a material less than $1nm$ thick, provide strong evidence for the exceptional sensitivity of our technique. The detection of a monolayer with simultaneous $10nm$ spatial resolution suggests that our volumetric sensitivity may be as good as $< 10 \times 10 \times 1nm$ for ultrathin conducting materials.

### 3.4.2 Observation of an Ultrathin Insulator

While the results of the previous section apply to ultrathin conductors, we also tested the capacity of our technique to measure ultrathin insulators. For this purpose, we chose to investigate the standard insulating oxide used by the semiconductor industry: thermally grown $SiO_2$ on Silicon substrate. The samples we used are commercially available AFM calibration gratings from NT-MDT:TGQ1 ($2nm$ & $22nm$), TGZ1 ($18nm$), TGZ2 ($108nm$), as well as one 300nm $SiO_2$ on Silicon wafer with trenches made in house. We recorded images over a broad range of IR frequencies: $\omega = 886 cm^{-1} - 2200 cm^{-1}$. Since all of the images also contained regions of Silicon, we were able to normalize the $SiO_2$ signals to Silicon at each frequency . In 3.3a we show $10nm$ resolved $S_3$ amplitude images of the $2nm$ & $22nm$ layers at three representative frequencies: $\omega = 1068 cm^{-1}, 1115 cm^{-1}, 1175 cm^{-1}$. All three images are normalized to the signal from the sample's exposed Silicon area and displayed with identical color scale. In this manner, we can immediately correlate colors brighter than Silicon to an enhanced signal and darker colors to suppression. This is evident for the center square area, known to be $22nm\ SiO_2$, which shows enhancement at $\omega = 1115 cm^{-1}$ and a suppression of the signal at $\omega = 1175 cm^{-1}$. The most surprising result however is the slight contrast between the $2nm$ oxide and Silicon at all frequencies shown. This cannot be due to topographical features since the $SiO_2$ regions have surface roughness virtually identical to that of the

Silicon region, $< 1nm$. A more likely explanation is that we are directly measuring the thickness-dependent reflection of the tip's evanescent field from the $SiO_2$ surface.

We confirm this hypothesis by performing a broadband spectroscopy study on $SiO_2$ samples with thicknesses from 2 to 300nm as shown in Fig.3.3. The spectra are generated by taking the ratio of the average signal between $1\mu m^2$ areas in the $SiO_2$ and Silicon regions of an image taken at each frequency. As we examine these spectra, the most noticeable effect is a large enhancement of the main $S_3$ maximum around $\omega = 1120cm^{-1}$ for all thicknesses, which subsequently decreases with thickness ,$d$, of the $SiO_2$ layer.

We can explain these effects by making an analogy between $S_3$ and the quasistatic p-polarized reflection coefficient, $r_p$. As we show in the supplementary material, the shape of a spectrum for normalized amplitude signals such as $\frac{S_3(SiO_2)}{S_3(Si)}$ very closely resembles $|\frac{r_p^{SiO_2}(q)}{r_p^{Si}(q)}|$ evaluated at some average field momentum generated at the tip apex: $\langle q \rangle \sim \frac{1}{R}$, where $r_p$ is the p-polarization Fresnel reflection coefficient. Since typical tip radii are $a \approx 25nm$, the evanescent field momenta produced by the tip are expected to be on the order of $q \sim (25nm)^{-1} \sim 400,000cm^{-1}$. Since the behavior of $S_3$ is in theory quite similar to quasistatic $r_p$, we do indeed expect large $S_3$ to be observed for frequencies in $SiO_2'$*s restrahlen* band, $\omega_{TO} < \omega < \omega_{LO}$, where $\omega_{TO} \approx 1070cm^{-1}$ and $\omega_{TO} \approx 1250cm^{-1}$ are the $SiO_2$ Transverse (TO) and Longitudinal (LO) phonon modes, respectively. This explains the increased $S_3$ relative to Silicon in this frequency region. We also expect thickness dependent $S_3$ behavior to be consistent with $r_p$ for a two layer system: as $d \to 0$ the reflection contribution of the top layer should systematically decrease. Furthermore, we can expect surface phonon excitation in the $SiO_2$ layer to become important for $qd \leq 1$ or $d < 25nm$, where $d$ is the thickness of the $SiO_2$ layer. We believe that this $qd$ dependence of $r_p$ is the key origin of the spectral shape for the thinner samples we studied.

We emphasize this point by showing 2 & $22nm$ thickness spectra in more detail in the insets of 3.3cd. The spectra clearly look consistent with the expected evolution of $r_p$ from $qd \approx 1$ to $qd \approx .1$ as shown in the Supp. Material. This is to be expected if the tips momentum does not change and the thickness does, by an order of 10, as we go from 2 to 22nm. In these spectra we also observe a prevalent secondary peak

around $\omega = 1180cm^{-1}$. We argue that this double peak structure can only be explained by a second TO mode with $\omega \approx 1160 - 1180cm^{-1}$. Our modeling results (shown in the supplementary material) confirm that this feature cannot be due to the subtleties of demodulation and indeed originates from the same physical origins which would cause such a feature to appear in the $r_p$ spectrum. The secondary phonon mode origin of this 2nd maximum agrees with previous measurements of thicker $SiO_2$ films where weaker, secondary phonon modes with $\omega_{TO} = 1164-1$ were observed[13]. Our ability to register this mode indicates a high degree of sensitivity to optical constants at the nanoscale.

Our results on ultrathin $SiO_2$ layers offer strong experimental support for the large momentum nature of a sSNOM probe. The implications for nanospectroscopy are quite promising. The $q \sim (25nm)^{-1}$ momenta make our technique somewhat analogous to performing spectroscopy using light of $\lambda \approx 10nm$ X-ray wavelength and IR frequency [2], a feat normally impossible in far-field optics. This simple analogy explains how we are able to easily observe contrasts for $2nm$ $SiO_2$ relative to Silicon and also spectroscopically differentiate $18nm$ from $22nm$ $SiO_2$. When coupled with the already demonstrated $10nm$ spatial resolution, these results demonstrate volumetric sensitivity as fine as $10 \times 10 \times 2nm$ to ultrathin insulating materials, such as amorphous $SiO_2$ layers.

## 3.5 Conclusion

The imaging and spectroscopy results presented here for the prototypical ultrathin conductor, suspended Graphene, and the representative ultrathin insulator, amorphous thermally grown $SiO_2$, showcase the utility of sSNOM for nanooptics measurements. The volumetric sensitivity achieved is as high as $< 10 \times 10 \times 2nm$ for both materials. We postulate that such sensitivity would not be attainable unless we are probing the reflection of evanescent waves with in-plane momenta $|q| > 400,000cm^{-1}$ over the entire IR frequency range of study, $886 - 2200cm^{-1}$. Since high momentum light implies high spatial frequencies, as a consequence we are able to spatially resolve nanoscale material properties, such as carrier density fluctuations in Suspended Graphene. The

[2] This of course applies at tip/sample distances on the order of $25nm$. Also, the reflection coefficients in our case are quasistatic

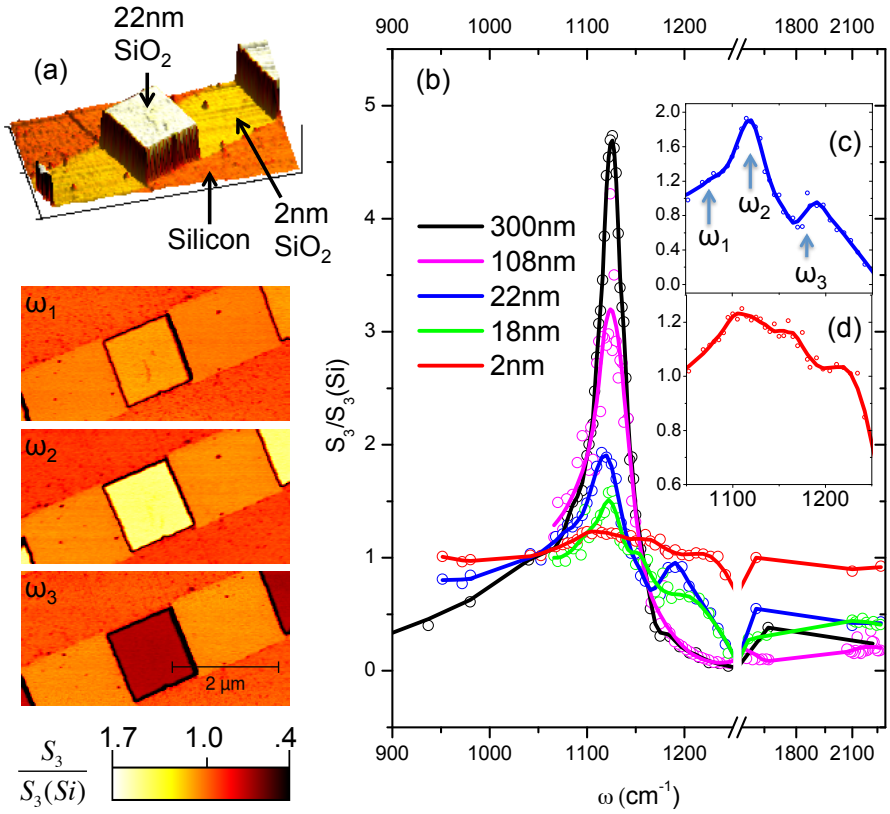


**Figure 3.3**: (a) $S_3$ images of $2, 22nm$ $SiO_2$ layers. Top image is a 3D projection of topography with the $S_3$ image at $\omega = 1115cm^{-1}$ overlaid. The contrasting regions corresponding to $2nm, 22nm$ and Silicon are indicated with arrows. Below this image is a set of $S_3$ images obtained at frequencies $\omega_{1,2,3} = 1068cm^{-1}, 1115cm^{-1}$, and $1175cm^{-1}$. All images have been normalized such that Silicon regions have the same color and signal level $S_3 = 1$. Nanospectra are shown in (b), obtained for all investigated thicknesses of $SiO_2$: 2, 18, 22, 108, and 300nm. These spectra are also normalized to Silicon such that their values are directly comparable to those displayed in the images. Insets (c) and (d) show detailed views of the $2nm$ and $22nm$ spectra, with arrows indicating frequencies of the images shown in (a).

remarkable sensitivity achieved with the sSNOM method should prove invaluable for any nanomaterial study where infrared frequencies are desirable for elucidating material properties.

## 3.6 Supplementary Material

### 3.6.1 Extended Monopole Model

The quantitative results presented in the main text were obtained with an analytic model of the near field interaction which we term the "Extended Monopole" model. The model accounts for both multilayered media and the geometry of the tip/nanonantenna. The tip is assumed to have an axially symmetric geometry, with a charge distribution resembling that of an elongated monopole. The bulk of the monopole's charge is heavily concentrated towards the tip apex. To account for the multilayer nature of the sample, we calculated the $q$-dependent reflection of the monopole's near fields, which we represent as a spectrum of plane waves. In this manner, any multilayer system's response is encapsulated in just the total reflection coefficient evaluated for each value of $q$. The effect of the reflected near fields on the tip's far field radiation is determined from the tip's effective dipole moment:

$$p \propto \frac{1}{1-\mathscr{G}} \tag{3.1}$$

where $\mathscr{G}$ is the integrated Green's function of the tip/sample system. We note that in previous works, a point dipole Green's function, $\mathscr{G} = a^3 G = a^3 \int dq q^2 r_p(q,\omega) e^{-2qz}$ was used, with $a$ being the tip radius and $z = a + \frac{A}{2}(1 + Cos(\Omega t))$ being the distance of the point dipole to sample, where $A$ is the tapping amplitude. In our experience, the results achieved by the dipole model tend to be qualitatively correct for many systems, but cannot reproduce important experimental details such as approach curves or resonance frequencies of phonon modes.

Our model is motivated by previous works [14][3] which showed that the apex of the polarized tip resembles a highly localized monopole far more than a point dipole. We also assumed that the only relevant dimensions are the tip radius $a$ and tip-sample

distance $z$ allowing the use of a quasistatic approximation since $a, z << \lambda$.These considerations led to the following integrated Green's function:

$$\mathscr{G} = a\int_0^\infty dq \frac{aq}{l+aq}\Lambda(q)r_p(q,\omega)e^{-2qz} \tag{3.2}$$

where $l$ is a charge localization coefficient, $\Lambda$ is the magnitude of charge induced in the tip at wavevector $q$, $r_p$ is the sample's p-polarization reflection coefficient, $z = z_{min} + \frac{A}{2}(1+cos(\Omega t))$ is the oscillating tip-sample distance, and $z_{min}$ is the minimum distance between the monopole's extent and the sample.

Since we demodulate the far field radiation collected from the tip, only those terms that vary harmonically with tapping frequency $\Omega$ are important. The final step in the calculation is then to demodulate the time dependent dipole moment expression 3.1 at the tapping frequency $\Omega$ as follows: $p_n = \int_{\frac{-T}{2}}^{\frac{T}{2}} p(t)Cos(n\Omega t)$. We compute this expression for two materials A and B, i.e. Graphene and Silicon, to arrive to the normalized experimental observables $S_n, \Phi_n$:

$$S_n = \left|\frac{p_{n,A}}{p_{n,B}}\right| \tag{3.3}$$

$$\Phi_n = |Arg\{p_{n,A}\} - Arg\{p_{n,B}\}| \tag{3.4}$$

### 3.6.2 Calculation of $S_n$ for Graphene

To calculate the expected near field signals for Graphene, we used a quasistatic approximation of the 2D Electron Gas reflection coefficient:

$$r_p = \frac{\varepsilon - 1 + 4\pi i\sigma_{2D}\frac{q}{\omega}}{\varepsilon + 1 + 4\pi i\sigma_{2D}\frac{q}{\omega}} \tag{3.5}$$

where $\varepsilon$ is the permittivity of the substrate and $\sigma_{2D}(\Gamma, E_f)$ is the conductivity of Graphene in the RPA approximation, described elsewhere[15]. For the case of Suspended Graphene referenced to Silicon, we use $\varepsilon = 1$,$\Gamma = 30cm^{-1}$ for calculating $r_p^{SG}$ and $r_p^{Si} = \frac{\varepsilon_{Si}-1}{\varepsilon_{Si}+1}$.

In 3.4 we show the calculated results for $\frac{S_{2,SG}}{S_{2,Si}}, |\Phi_{2,SG} - \Phi_{2,Si}|$ at the frequency $\omega = 1192cm^{-1}$. The $S_2$ and $\Phi_2$ experimental data are represented by the blue and pink shaded bars respectively, centered vertically at the average $S_2$ or $\Phi_2$ signal. The vertical extent of the bars represents the standard deviation of each signal, determined from the width of the image histograms(inset). By imposing the constraints of experimental

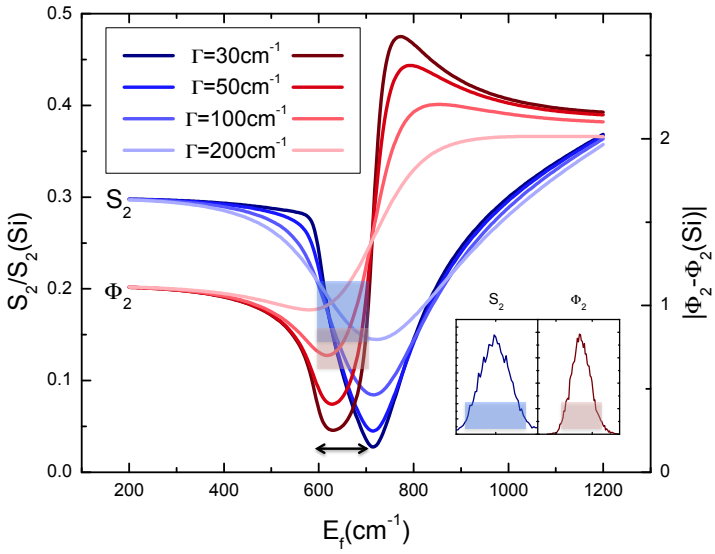


**Figure 3.4**: Normalized $S_2, \Phi_2$ values for Suspended Graphene at $\omega = 1192cm^{-1}$ vs. $E_f$ calculated using the Extended Monopole model for several choices of $\Gamma$. The range of experimentally observed $S_2, \Phi_2$ values are represented by the vertical extent of the blue, pink shaded regions respectively. The horizontal extent of the shaded regions is determined by their total intersection with the theoretical curves. The resultant predicted range in $E_f$ is marked by the double arrow.

amplitude and phase data on the theoretical plots, we are able to restrict the range of possible $E_f$ and $\Gamma$ values. This allows us to approximate the Fermi Energy distribution in the suspended Graphene to be: $600 \leq E_f \leq 700 cm^{-1}$ and the scattering rate to be in the range of: $50 cm^{-1} \leq \Gamma \leq 150 cm^{-1}$.

### 3.6.3 Application to thin resonant layers such as $SiO_2$

In the main text we mention several key aspects of the near field response of a $SiO_2$ layer with thickness $d$:

i. $\frac{S_n^{SiO_2}}{S_n^{Si}}$ essentially scales with $\left| \frac{r_p^{SiO_2}(q)}{r_p^{Si}(q)} \right|$ where $\langle q \rangle \sim \frac{1}{a}$

ii. Contrast in the $\frac{S_n^{SiO_2}}{S_n^{Si}}$ spectrum decreases with $d$

iii. A weaker, secondary TO mode is needed to explain $S_n$ for $qd < 1$

Similar to the expression for Graphene on $SiO_2$ we can write down the quasistatic, $q >> \frac{\omega}{c}$ TM reflection coefficient for the two layer system of thin $SiO_2$ on Silicon substrate:

$$r_p = \frac{\rho_1 + \rho_2 e^{-2qd}}{1 + \rho_1 \rho_2 e^{-2qd}} \tag{3.6}$$

$$\rho_1 = \frac{\varepsilon_{SiO_2} - 1}{\varepsilon_{SiO_2} + 1} \tag{3.7}$$

$$\rho_2 = \frac{\varepsilon_{Si} - \varepsilon_{SiO_2}}{\varepsilon_{Si} + \varepsilon_{SiO_2}} \tag{3.8}$$

The thickness dependence of the sample enters the equations in only one place, as an exponential term arising from an infinite number of multiple reflections within the layer. The effect of this term on the $r_p$ coefficient is illustrated in Fig.3.5. In panels (a) and (b) we calculate $r_p$ for successive values of $qd$ ranging from $.1 - 10$. We also vary the number of lorentzian oscillators used to model the $SiO_2$ permittivity, 2 primary oscillators are utilized in panel (a) while three are used in panel (b). For either case, we see that the reflection of the two-layer system is always approaching the reference value of $r_p(Si)$ as $qd$ is decreased. In experiment, $\langle q \rangle$ of the tip remains roughly the same while $d$ is changing.. For the two cases of 2 & $22nm$ $SiO_2$ and a tip radius of $a \sim 25nm$ we expect $qd \sim .1$ and $qd \sim 1$ respectively to be the most representative, assuming $\langle q \rangle \sim \frac{1}{a}$.

In plots 3.5cd we show the calculated $S_3$ values for the same set of optical constants used for panels a,b. These plots verify claim [i] above, that the qualitative behavior of $S_3$ appears virtually identical to that of normalized $r_p$ at the proper $qd$ values: $qd = .1$ and $qd = 1$. The second claim is reproduced as well, as is clear from either the behavior of decreasing $S_3$ contrast with decreasing $d$, or equivalently the decreasing $r_p$ contrast for decreasing $qd$. Lastly, we also verified claim [iii] by comparing the shapes of the calculated spectra for either the two or three oscillator case (Fig. 3.5cd) to the experimental data shown in the insets of Fig.3 in the main text. The two oscillator case does not reproduce the experimentally observed additional maximum in the spectra for both 2 and 22$nm$ cases. Neither the $r_p$ or $S_3$ spectra shown in panels a,d appear like experiment. We therefore conclude that the secondary maximum in experimental data originates from an additional, secondary phonon mode with $\omega_{TO} \approx 1180 cm^{-1}$

In Table 3.6.3 we summarize the best fit parameters obtained with the Extended Monopole model for all of the $SiO_2$ shown in this work. The $SiO_2$ permittivity can be calculated from these values according to $\varepsilon = \varepsilon_\infty + \Sigma_{n=1}^{N} \frac{s_n \omega_n \Gamma_n}{\omega_n^2 - \omega^2 - i\Gamma_n \omega}$.

## 3.7 Acknowledgements

The author would like to thank the co-authors of this publication for allowing its usage in this dissertation:

G. O. Andreev, Z. Fei, A. S. McLeod, W. Bao, L. M. Zhang, A. Castro-Neto, Z. Zhao, G. Dominguez, M. Thiemens, M. M. Fogler, C. N. Lau, F. Keilmann, and D. N. Basov. "Infrared nanooptics of ultrathin materials." (in preparation), 2011.

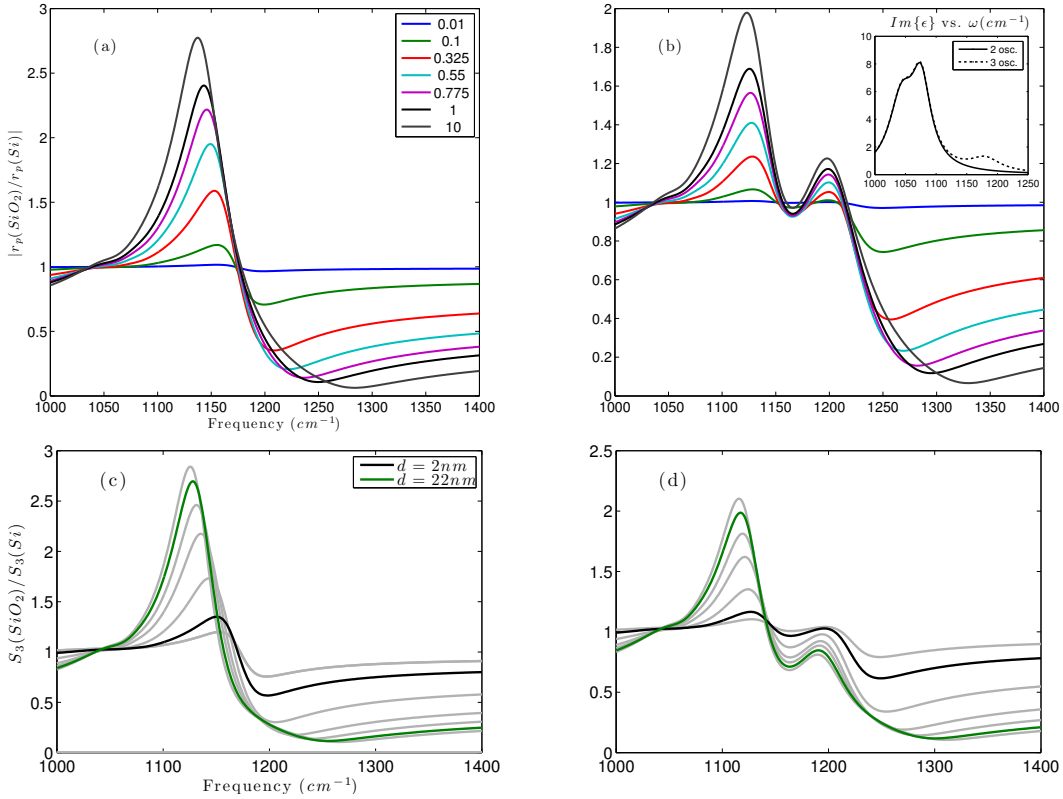


**Figure 3.5**: $\left|\frac{r_p^{SiO_2}(q)}{r_p^{Si}(q)}\right|$ plotted for $qd = .01 - 10$ for a choice of either two or three primary oscillators in modeling the $SiO_2$ permittivity in this frequency range (panels (a),(b) respectively). In the inset of panel (b) the imaginary part of the 2 and 3 primary oscillator $SiO_2$ permittivities is shown. Panels (c) and (d) show the calculated $S_3$ values using the Extended Monopole model with the same 2 or 3 main oscillator $SiO_2$ parameters, respectively. The gray curves are $S_3$ calculated for the thicknesses $d = 1, 5, 10, 15, 30$ in increasing order. The experimentally relevant curves, $2nm$ and $22nm$, are qualitatively very similar to the $qd = .1$ and $qd = 1$ $R_p$ plots in panels (a) and (b).

**Table 3.1**: Fitting parameters for $SiO_2$ using the Extended Monopole model. Manufacturer's stated thickness is shown in parentheses. The model parameters were $z_{min} = .5R, R = 50nm, \lambda_0 = 1.4, l = 2, A = 50nm$.

| $SiO_2$ Thickness | $\varepsilon_\infty$ | $f_1$ | $f_2$ | $f_3$ | $f_4$ | $\omega_1$ | $\omega_2$ | $\omega_3$ | $\omega_4$ | $\Gamma_1$ | $\Gamma_2$ | $\Gamma_3$ | $\Gamma_4$ |
|---|---|---|---|---|---|---|---|---|---|---|---|---|---|
| **2.8 (2)** | **1.8** | **0.3** | **9.2** | **5.0** | **0.7** | **830.0** | **1030.0** | **1060.0** | **1183.2** | **99.9** | **59.5** | **15.0** | **100.0** |
| 20 (18) | 1.9 | 0.2 | 6.1 | 5.0 | 0.7 | 808.7 | 1059.3 | 1087.0 | 1170.9 | 59.8 | 27.1 | 41.2 | 99.2 |
| **20.8 (22)** | **2.0** | **0.001** | **5.0** | **6.1** | **1.0** | **810.3** | **1043.7** | **1075.6** | **1180.4** | **15.0** | **49.4** | **39.0** | **60.2** |
| 108 (108) | 2.2 | 0.03 | 8.0 | 6.6 | 0.4 | 802.5 | 1060.0 | 1088.3 | 1167.3 | 19.2 | 34.9 | 42.2 | 57.6 |
| 300 (300) | 1.9 | 0.3 | 8.0 | 8.0 | 0.3 | 830.0 | 1060.0 | 1090.6 | 1148.3 | 94.2 | 29.6 | 25.2 | 45.7 |

# Bibliography


[1] Joel Gersten and Abraham Nitzan. Electromagnetic theory of enhanced raman scattering by molecules adsorbed on rough surfaces. 73(7):3023–3037, 1980.

[2] Javier Aizpurua, Thomas Taubner, F. Javier García de Abajo, Markus Brehm, and Rainer Hillenbrand. Substrate-enhanced infrared near-fieldspectroscopy. *Opt. Express*, 16(3):1529–1545, Feb 2008.

[3] A. Cvitkovic, N. Ocelic, and R. Hillenbrand. Analytical model for quantitative prediction of material contrasts inscattering-type near-field optical microscopy. *Opt. Express*, 15(14):8550–8565, Jul 2007.

[4] Markus Brehm, Thomas Taubner, Rainer Hillenbrand, and Fritz Keilmann. Infrared spectroscopic mapping of single nanoparticles and viruses at nanoscale resolution. *Nano Letters*, 6(7):1307–1310, 2006.

[5] A. J. Huber, A. Ziegler, T. Kock, and R. Hillenbrand. Infrared nanoscopy of strained semiconductors. *Nat Nano*, 4(3):153–157, March 2009.

[6] M. M. Qazilbash, M. Brehm, Byung-Gyu Chae, P.-C. Ho, G. O. Andreev, Bong-Jun Kim, Sun Jin Yun, A. V. Balatsky, M. B. Maple, F. Keilmann, Hyun-Tak Kim, and D. N. Basov. Mott transition in vo2 revealed by infrared spectroscopy and nano-imaging. *Science*, 318(5857):1750–1753, 2007.

[7] Markus B. Raschke, Leopoldo Molina, Thomas Elsaesser, Dong Ha Kim, Wolfgang Knoll, and Karsten Hinrichs. Apertureless near-field vibrational imaging of block-copolymer nanostructures with ultrahigh spatial resolution. *ChemPhysChem*, 6(10):2197–2203, 2005.

[8] Thomas Taubner, F. Keilmann, and R. Hillenbrand. Nanoscale-resolved subsurface imaging by scattering-type near-field optical microscopy. *Opt. Express*, 13(22):8893–8899, Oct 2005.

[9] F. Huth, M. Schnell, J. Wittborn, N. Ocelic, and R. Hillenbrand. Infrared-spectroscopic nanoimaging with a thermal source. *Nat Mater*, 10(5):352–356, May 2011.

[10] J. Martin, N. Akerman, G. Ulbricht, T. Lohmann, J. H. Smet, K. von Klitzing, and A. Yacoby. Observation of electron-hole puddles in graphene using a scanning single-electron transistor. *Nat Phys*, 4(2):144–148, February 2008.

[11] Mario F. Borunda, Jesse Berezovsky, Robert M. Westervelt, and Eric J. Heller. Imaging universal conductance fluctuations in graphene. *ACS Nano*, 5(5):3622–3627, 2011.

[12] Stephane Berciaud, Sunmin Ryu, Louis E. Brus, and Tony F. Heinz. Probing the intrinsic properties of exfoliated graphene: Raman spectroscopy of free-standing monolayers. *Nano Letters*, 9(1):346–352, 2009.

[13] Marta Klanjsek Gunde. Vibrational modes in amorphous silicon dioxide. *Physica B: Condensed Matter*, 292(3-4):286 – 295, 2000.

[14] Lukas Novotny, Erik J. Snchez, and X. Sunney Xie. Near-field optical imaging using metal tips illuminated by higher-order hermite-gaussian beams. *Ultramicroscopy*, 71(1-4):21 – 29, 1998.

[15] Z. Fei, G. O. Andreev, W. Bao, L. M. Zhang, A. S. McLeod, A. Castro-Neto, Z. Zhao, G. Dominguez, M. Thiemens, M. M. Fogler, C. N. Lau, F. Keilmann, and D. N. Basov. Dirac plasmons at the graphene-sio2 interface. *(submitted)*, 2011.

# 4 Construction of a Cryogenic Infrared Nanoscope

## 4.1 Introduction

At low temperatures, a rich array of yet to be understood physics awaits experimenters possessing the right tool for the job. One such tool, which until now was unavailable, is a microscopy method capable of nanoscale infrared imaging and spectroscopy in cryogenic conditions. Some systems that are ripe for such study include: superconductors, correlated oxides, or polariton Bose Einstein Condensates [1][2][3]. Nanoscale infrared investigations of these interesting systems have yet to be performed at their transition temperatures. Our previous sSNOM measurements of similar compounds [4] at elevated temperatures indicate that such transitions can indeed be observed with sSNOM. For this reason, one of the first experiments we tried with the completed cryo-sSNOM was to look at the transition of a compound closely related to $VO_2$: $V_2O_3$. Our first results on the correlated oxide $V_2O_3$ indeed show a transition qualitatively very similar to $VO_2$. These are presented in the last section of this chapter.

## 4.2 Design

The primary considerations which went into the design of our cryo-sSNOM instrument were the necessary vacuum level, vibration tolerance, choice of cryogenic system, and optical coupling. Each of these is an important parameter which can heavily influence the overall choice of cryo-sSNOM design. For us, UHV conditions and Liquid

Helium cooling of the sample were a necessity. Ultimately, these two factors led to the layout of the completed system shown in Fig. 4.1 - 4.2. In the sections below, we detail the reasoning behind these and other design choices.

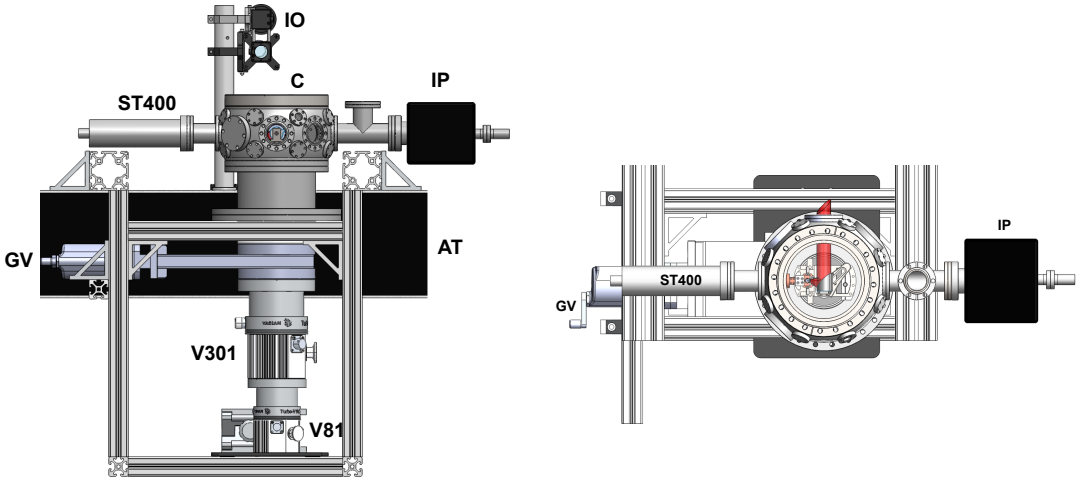


**Figure 4.1**: Side and top views of the cryo-sSNOM system. C = chamber, IO = Inspection Optics, IP = Ion Pump, ST400 = cryostat, AT = Air Table, V301 = large turbo pump, V81 = smaller backing turbo pump, GV = gate valve.

### 4.2.1 Vacuum levels

One of the main issues in cryogenic surface science is the formation of superficial nanometers-thick ice layers on the sample surface for $T < 150K$[1]. The ice layer can be especially problematic for techniques such as AFM, STM, and SNOM, where the properties of the sample's topmost nanometer can be important. In previous studies, it was shown that the ice layer can be avoided if one achieves pressure levels on the order of $P < 10^{-8}mbar$, which falls into the realm of Ultra High Vacuum (UHV). To achieve UHV pressures it is necessary to raise the temperature of the chamber in a process called "baking". Baking is done so that the absorbed water layers can be evaporated and pumped out. A typical bake may last for 24 hours with a constant temperature of $T = 100C$ maintained throughout the chamber. Afterwards, pressures below $10^{-10}$mbar can be achieved if no outgassing takes place inside the chamber. The low outgassing

[1]We measured the freezing point of water in our setup to be $148.6K$ at $P = 10^{-7}mbar$

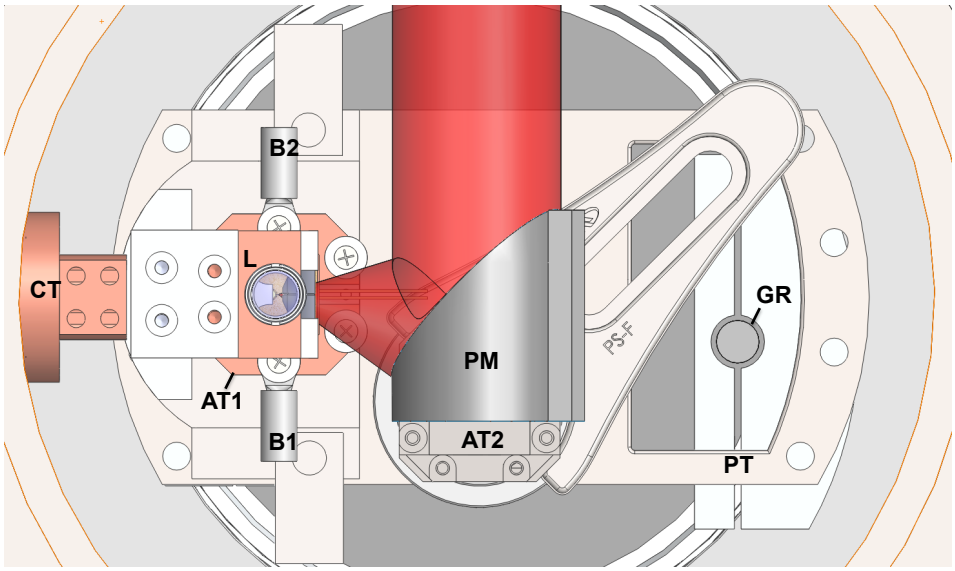


**Figure 4.2**: Detailed view of the chamber interior. CT = cryostat (cold finger), L = lens, AT1 = attocube stack 1, B1 = braid connector, B2 = braid connector, PM = parabolic mirror, AT2 = attocube stack 2, PT = platform, GR = glass rod coupling. For cooling the sample, flexible copper braids (not shown) are attached from CT to B1 and B2.

requirement greatly limits the range of materials which are deemed ”UHV compatible”. For instance, the oil from human skin leaves an outgassing residue on all materials that prevents UHV pressures from being reached sometimes even after baking. Also, it goes without saying that everything put inside a UHV chamber must be able to survive the highest baking temperatures. These requirements rule out many common materials such as plastics, adhesives, rubbers, and some types of electrical solder. Materials that are compatible include: pure glass, annealed copper, certain stainless steel alloys, titanium, kapton, and most ceramics. For a full list of materials sorted by outgassing properties, one may refer to the NASA database at outgassing.nasa.gov.

### 4.2.2 Choice of AFM

Given the material considerations outlined above, we needed an AFM as well as a stack of XYZ positioners for the parabolic mirror made of UHV compatible materials. For both we went with the company Attocube Inc. due to the compact size and full UHV compatibility of their positioners. We chose to start with their UHV low-

temperature AFM and modify it to work as a cryo-sSNOM. Out of the box, the Attocube AFM is an extremely compact device (see AT1 Fig. 4.2) that utilizes all UHV compatible components: titanium for the positioners, kapton for the electrical insulation, and a glass/polyimide single-mode fiber optic. The fiber is used for topography readout as an alternative to the common laser deflection method. The latter scheme contains several components which are typically not UHV compatible: photodetector, laser, and the necessary electrical circuitry.

In the fiber optic detection scheme, the position of the cantilever is read out by measuring the Fabry Perot interference pattern formed between the backreflection from the flat end of the fiber (F) and a reflection from the cantilever surface (CT) as shown in Fig.4.3 [5]. In this approach, only the fiber needs to be inside the UHV space. For readout, it is coupled to a fiber optic feedthrough which delivers the backreflected light to an external detector. The attocube AFM was one of the few systems on the market utilizing this technique. An alternative UHV compatible approach that we are also aware of is to use tuning fork methods for oscillating the tip. We did not pursue this direction because of the relatively small tapping amplitudes achievable. For sufficient modulation of the near field signals we require at least a $30nm$ tapping amplitude, which to our best knowledge is not yet achievable using tuning forks.

The attocube AFM also utilizes sample scanning for imaging instead of tip scanning. For our purposes, it is highly desirable that the tip stays stationary once we have focused the external light onto its apex. If the tip were to move, we would be forced to dynamically realign our optics to track the tip, which is a very difficult procedure.

Another feature which we found to be absolutely crucial is the addition of top inspection optics to the Attocube AFM. We achieved this by modifying the cantilever head assembly to house a small, 8mm diameter, NA=0.2 lens, shown as L in Fig.4.2. The lens' focus is adjusted to lie just above the cantilever so that an intermediate image plane is formed outside of the chamber. Externally, we can then use a second lens to collect light from this point, magnify it, and bring it onto a CCD camera with an additional inspection optics assembly, marked IO in Fig. 4.1. The resolution achievable with these inspection optics is on the order of $3\mu m$, which could use improvement in a future redesign. The main purpose of the inspection optics was achieved: to allow a

large field of view for optical alignment of the external light source.

Lastly, another major requirement is that the AFM must be open to optical access by external light. After some slight modification, the attocube AFM was fully compatible with incidence angles up to 40° as illustrated in Fig.4.3.

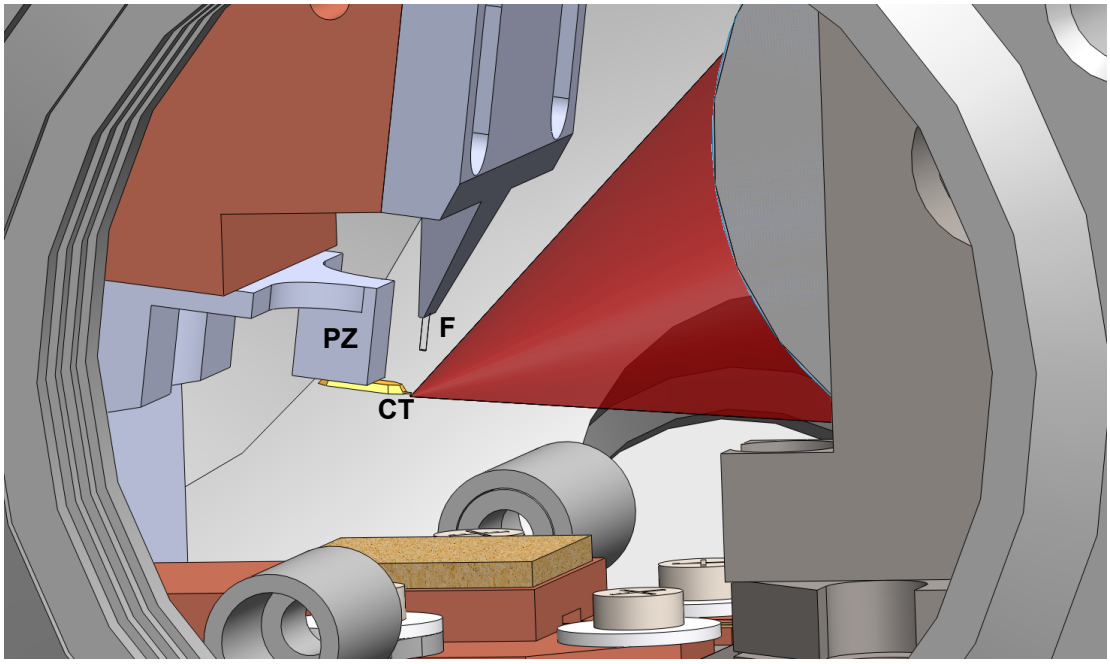


**Figure 4.3**: Detailed view of the AFM cantilever, CT, the fiber optic F, and the piezo PZ used to modulate the cantilever.

### 4.2.3 Vibration Isolation

The second major hurdle faced by any scanning probe method is that of excessive vibrations ruining AFM performance. This issue exists whether in vacuum or ambient conditions.

We solved this problem in several steps. We eliminated major vibrations from the immediate environment by attaching the vacuum chamber to a floating air table using a rigid $2 \times 2in$ unistrut frame, shown in 4.1. Due to the ultralow resonance frequency as well the large mass of the optical table, most of the building vibrations are heavily damped. All that remains are vibrations originating from equipment which is already in contact with the table itself. This includes laser electronics, vacuum pumps, and

the cryostat. Each of these, if not handled properly, adds sufficient noise to ruin AFM performance.

Vibrations from the laser electronics were perhaps the easiest to remove. We did this by opting not to use the standard fans utilized to cool laser housings, and instead employed water cooling for all of our lasers. We found this to significantly reduce noise in the $30-60Hz$ range where fans normally operate.

The mechanical noise from the turbopumps and rotary pumps was eliminated by switching to a combination of Ion pumping and cryopumping when sufficient vacuum levels have been reached. As described in the previous section, a UHV gate valve is used to isolate the mechanical pumps from the rest of the system. After this is done, they can be turned off.

The last source of significant vibrations in our setup occurred in the thermal coupling of the sample stage to the cryostat. In our design, the thermal contact is made via flexible copper braids mounted from the cryostat cold finger attachment (CT) to braid connectors on both sides of the sample stage (B1 and B2) as shown in Fig. 4.2. In this manner, the weight of the braids is distributed equally on the AFM scanner. Also, it is worth noting that the braids must be light in order to not interfere with the scanning. Any asymmetric tension may warp the AFM image. We determined that the main source of vibrations coupling through the braids was due to Helium boil-off at the cryostat cold finger. Surprisingly, we did not experience significant vibrations from the mechanical coupling of the transfer line to the Helium dewar. Once we identified the source of the vibrations, the solution was simple: minimize the flow of Helium to the cryostat cold finger. We achieved this by fine control of a needle valve in the Helium transfer line. By keeping the flow at a minimum, the vibrations were minimized to sub nanometer levels.

### 4.2.4 Cryogenics

For our desired study of superconductors and transitions in correlated oxides, a temperature range from $T = 4.2K - 300K$ was sufficient. To reach these temperatures, we chose a UHV liquid $He^4$ flow cryostat, the ST-400 from Janis. The cryostat utilizes a needle valve transfer line design allowing fine control of the helium flow, which is critical to minimizing vibrations. The cooling power of the cryostat is $.5W$ at 4.2K with

a Helium consumption of just under half a liter per hour. We found that its performance remained superb even while mounted horizontally.

As mentioned previously, the cryostat is connected to the sample via flexible copper braids (CT to B1,B2 4.2). The braids provide cooling while still allowing the sample scanner to move. Beneath the sample stage we place some thermal insulation in the form of ceramic cylinders. In this manner we do not cool the rest of the microscope. As a precaution, the rest of the microscope is isolated from the warm chamber by glass rods which support the stainless steel platform that it rests on (GR and PT in Fig.4.2.

### 4.2.5 Vacuum Chamber

The chamber which contains the microscope was built around a commercially available design from Kimbel Physics Inc., with 8 CF2.75, 16 CF1.25 (side), and 2 CF8 ports (top and bottom) (C in Fig.4.1). Each port is sealed using annealed copper gaskets, which must be replaced during each pump down. A glass window was placed on the top port to allow us to inspect the sample from above. The CF2.75 port towards the optical table houses an optical window, typically of a 1" broadband ZnSe material. We utilized 5 more of the CF2.75 ports for the following: electrical feedthroughs ($\times 2$), Ion Gauge and Ion Pump, optical window for side inspection, and cryostat. The bottom CF8 port of the chamber couples via an extension to a UHV Gate Valve (VAT Inc.) marked GV in Fig.4.1. Below the gate valve we connected two turbo pumps in series, the powerful V301 and the smaller V81 (Varian Inc.). The V81 is then connected to a Rotary pump via bellows and a long stainless steel pipe (not shown in the Figures).

### 4.2.6 Optical Coupling

Perhaps the most important consideration is the method for coupling external light to the AFM tip for near field generation. Our approach was to place an off-axis parabolic mirror inside the chamber, on a UHV compatible XYZ piezo stage (also from Attocube) equipped with a position readout (see PM and AT2 in 4.2. The use of a mirror avoids chromatic aberrations and does not require antireflection coatings for optimal performance. The main disadvantage however is the difficulty of alignment, especially

in finding the optical axis of the parabola. To accomplish this we developed a simple procedure, described in the Appendix, involving the use of a flat mirror attached to the back of the parabola.

Externally, without any modifications, the optics mimic the previously described pseudoheterodyne setup used by other sSNOM groups [6]. The only additional element in our setup is a broadband ($\lambda = 4 - 12\mu m$) antireflection-coated ZnSe window for the external light entering the chamber. While this window does limit the overall frequency range of the system, it can be easily replaced with a more suitable choice for experiments at other frequencies, such as visible or THz.

## 4.3 Imaging results on $V_2O_3$ for $T = 80 - 300K$

To demonstrate the performance of the instrument, we show some preliminary results on the metal to insulator transition in $V_2O_3$. As shown in the resistivity plot in 4.4, a 6 orders of magnitude transition takes place around $T = 150K$. At IR frequencies, the transition manifests itself as a decrease in reflection with lower temperatures. Our previous sSNOM results on $VO_2$ indicated the onset of percolation. The first cryo-sSNOM results that we have obtained on $V_2O_3$ however do not show this to be the case. It appears that the material transitions without percolation.

Below, we present our preliminary results for $S_2$ amplitude acquired at the IR frequency of $\omega = 1110cm^{-1}$. All of the data were obtained using 70nm tapping amplitude. The color scale range is kept the same for all images. The first set of images were obtained as the temperature was decreased (Fig. 4.5) while the second set was during warming up of the sample (Fig. 4.6). The two sets clearly differ from each other for the intermediate temperatures such as 125K-150K. Here, the warming up data sequence appears more insulating at the same temperatures. This is a clear sign of hysteresis. To confirm that the transition is consistent we also took one more image at 86K after the down/up cycle shown in Fig.4.54.6 was completed. This image is again consistent with the insulating signals observed for $T < 125K$. We believe these early results demonstrate that the cryo-sSNOM is indeed functional and can already reveal some interesting physics.

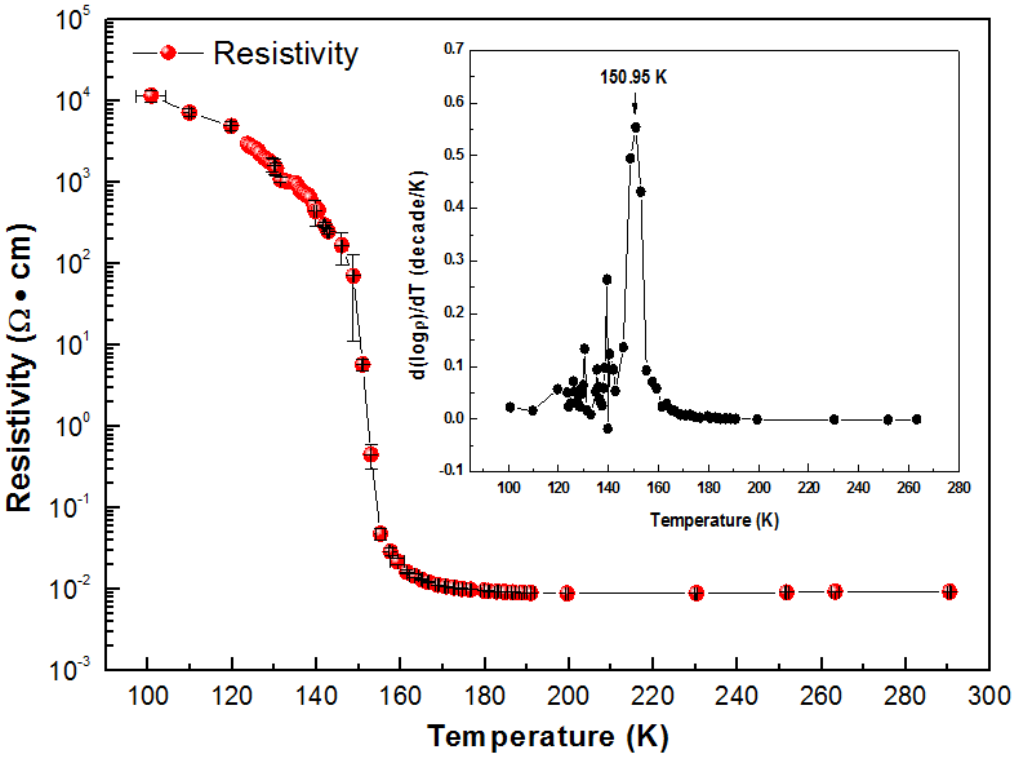


**Figure 4.4**: Resistivity vs. Temperature plot for a $V_2O_3$ thin film on Sapphire substrate. The data were obtained while heating up, after the sample had cooled.

## 4.4 Appendix

### 4.4.1 Optical Alignment procedure

To avoid severe coma aberations inherent to parabolic mirrors, it is necessary to insure that the light is incident along the optical axis of the parabola. We accomplish this by aligning the external beam to a small flat mirror which has been mounted to the back of the parabola (FM in Fig. 4.2 and Fig. 4.7) such that it reflects incident light exactly along the parabola's optical axis. A mirror external to the chamber is used to control the angle of the beam so that it returns along the same path. After this is achieved, the external mirror is translated laterally ($\Delta x$ Fig. 4.7) so that the beam is incident on the parabola once again. Next, the XYZ positioners can be utilized to bring the beam onto the AFM tip. This step can be rather tedious. Assuming a visible laser in parallel with the external light source is available, a helpful procedure is to place a roughened sample

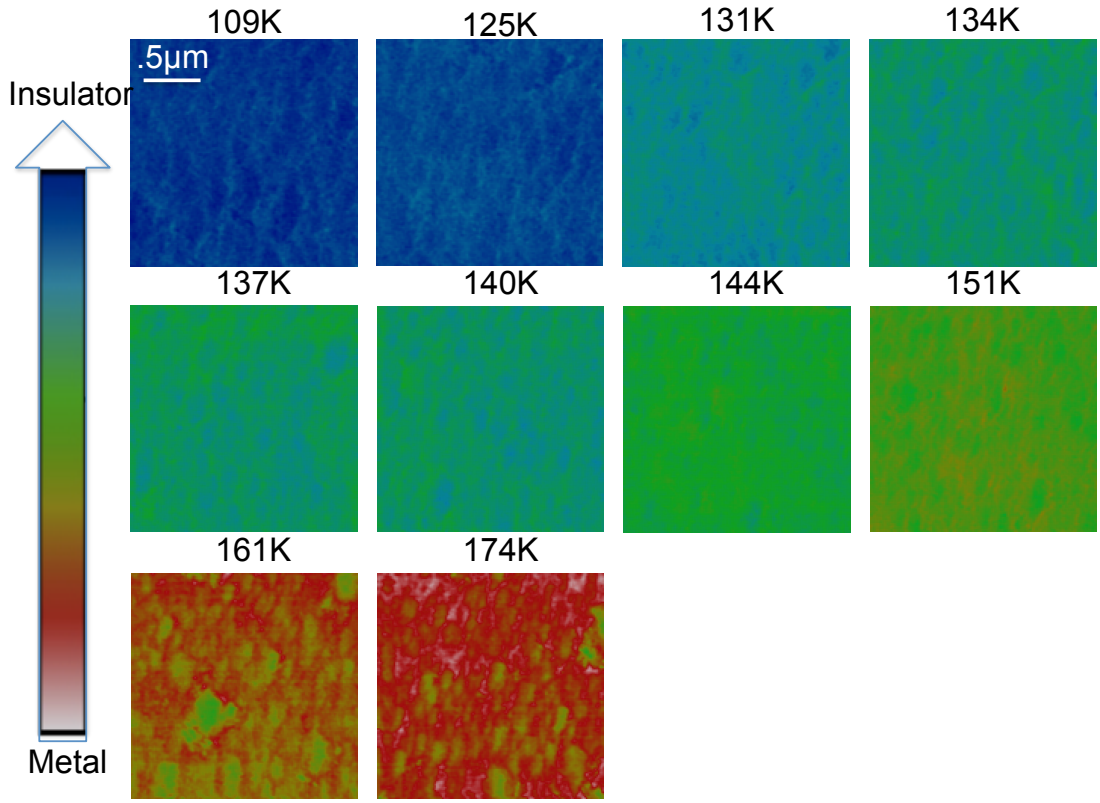


**Figure 4.5**: $2 \times 2\mu m$ cryo-sSNOM amplitude ($S_2$) images of $V_2O_3$ normalized to the signal at $T = 190K$. As it cools, it undergoes a metal ($T = 190K$) to insulator ($T = 109K$) transition as judged from the observed loss of signal.

surface under the tip and monitor the backscattered light with inspection optics from above. The visible laser spot can be used to find the proper focus and position of the external light beam, since it is parallel to the visible one.

### 4.4.2 Pumpdown procedure

In order to obtain UHV vacuum levels as quickly as possible, we utilized a 6 stage pump-down procedure involving a Rotary Pump , two turbomolecular pumps (V81 and V301 Varian), an Ion pump and optionally, the cryopumping action of the cryostat. After all chamber ports have been sealed, we perform the following pumpdown procedure:

i Start the Rotary pump, with gate valve open. When pressure reaches below 1mbar

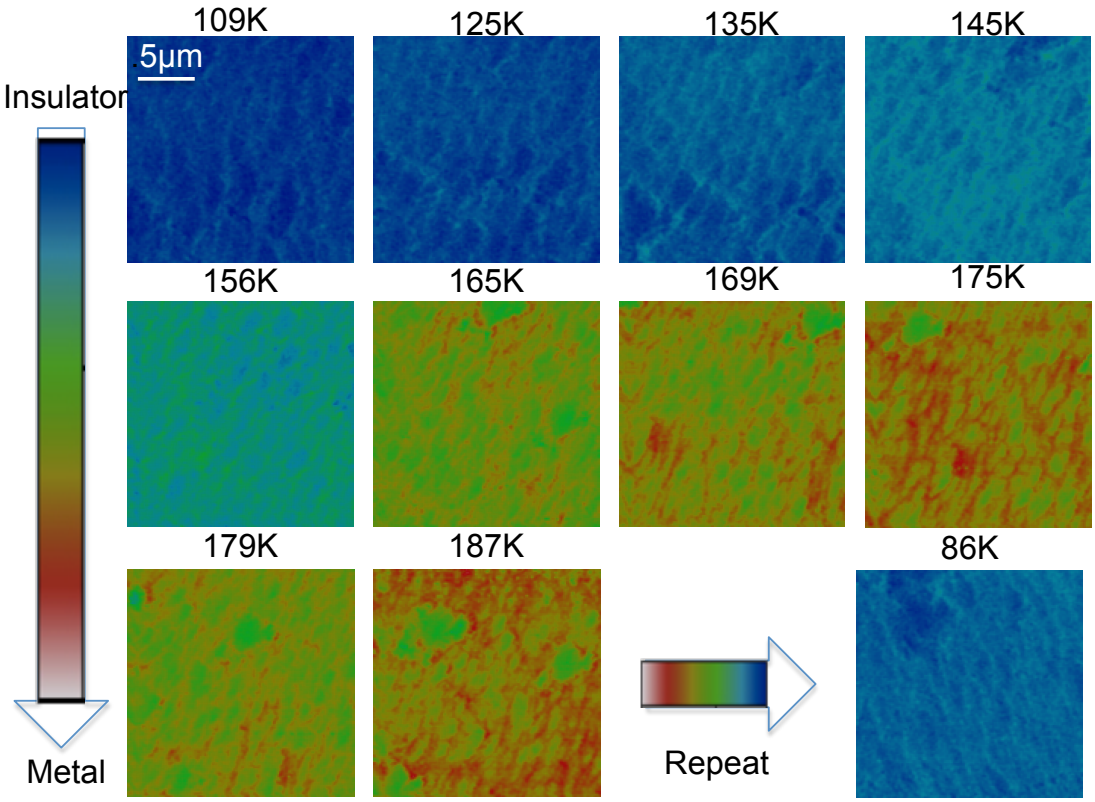


**Figure 4.6**: $2 \times 2\mu m$ amplitude ($S_2$) images of the same $V_2O_3$ sample, now warmed up. $V_2O_3$ undergoes an insulator ($T = 190K$) to metal($T = 109K$) transition. To check for consistency we then quickly cooled the sample back to $86K$ and recovered the level of signal from the insulating phase.

proceed to the next step.

ii Turn on the V81, wait until it reaches full speed and then turn on the T301. Turn on the ion gauge. If the system does not have major leaks the vacuum should be below $10^{-4}$mbar within 5 minutes. Perform a leak test if needed.

iii Once the pressure is at $10^{-5}$mbar, the ion pump can be turned on. Initially, the pressure may rise due to some previously trapped material being released within the pump. If this occurs, turn the pump off and on several times until the effect is gone.

iv Start the baking process by turning on the heating elements attached all around

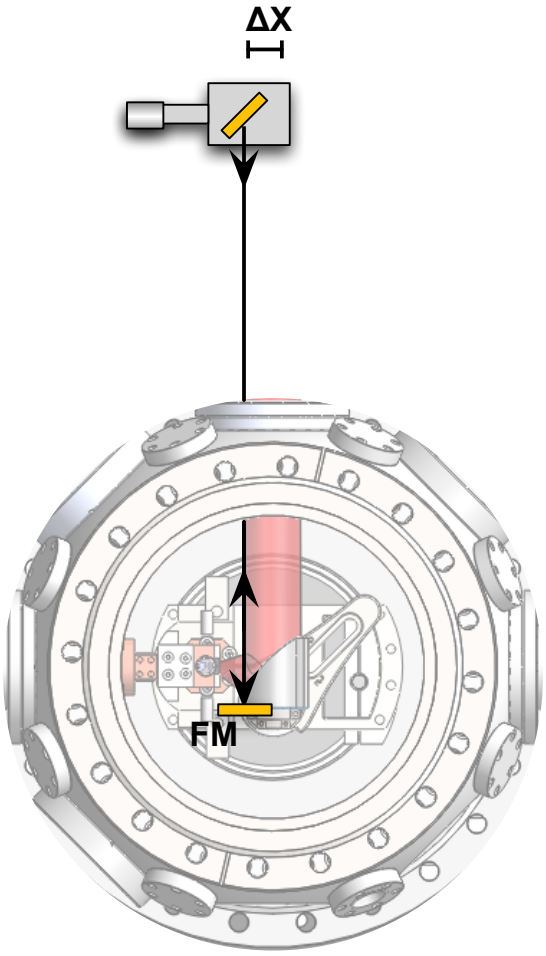


**Figure 4.7**: Detailed view of the AFM cantilever, CT, the fiber optic F, and the piezo PZ used to modulate the cantilever.

the chamber. Shield chamber with foil if high bakeout temperatures are needed. Bake for a minimum of 24 hours.

v Turn off heaters. Once the chamber is again at room temperature the pressure should be below $5 \times 10^{-8} mbar$. Close and open the gate valve to make sure the ion pump is working.

vi Insert cryostat transfer line and cool the cryostat below $T < 150K$. The pressure will drop immediately as water condenses on the cryostat's cold finger. It is recommended that the sample temperature be kept above $200K$ to avoid ice formation during this cryopumping process. Once the vacuum levels stabilize you may pro-

ceed to close the gate valve, turn off the turbo pumps, turn off the Rotary pumps and begin measurements. Alternatively you can measure without cryopumping, although in this case the vacuum levels may be higher.

Following this procedure we can maintain pressure levels below $P < 10^{-8} mbar$ with just the ion pump and cryopumping action alone. This is highly desirable since any sort of mechanical pumping introduces intolerable vibrations. In our setup, we measure these vibrations to be at least 5nm.

# Bibliography


[1] G. Lang, H.-J. Grafe, D. Paar, F. Hammerath, K. Manthey, G. Behr, J. Werner, and B. Büchner. Nanoscale electronic order in iron pnictides. *Phys. Rev. Lett.*, 104(9):097001, Mar 2010.

[2] M. M. Qazilbash, A. A. Schafgans, K. S. Burch, S. J. Yun, B. G. Chae, B. J. Kim, H. T. Kim, and D. N. Basov. Electrodynamics of the vanadium oxides $vo_2$ and $v_2o_3$. *Phys. Rev. B*, 77(11):115121, Mar 2008.

[3] J. Kasprzak, M. Richard, S. Kundermann, A. Baas, P. Jeambrun, J. M. J. Keeling, F. M. Marchetti, M. H. Szymanska, R. Andre, J. L. Staehli, V. Savona, P. B. Littlewood, B. Deveaud, and Le Si Dang. Bose-einstein condensation of exciton polaritons. *Nature*, 443(7110):409–414, September 2006.

[4] M M Qazilbash, M Brehm, B G Chae, P C Ho, G O Andreev, B J Kim, S J Yun, A V Balatsky, M B Maple, F Keilmann, H T Kim, and D N Basov. Mott Transition in VO2 Revealed by Infrared Spectroscopy and Nano-Imaging. *Science*, 318(5857):1750–1753, dec 2007.

[5] D. Rugar, H. J. Mamin, and P. Guethner. Improved fiber?optic interferometer for atomic force microscopy. *AIP*, 55(25):2588–2590, 1989.

[6] Nenad Ocelic, Andreas Huber, and Rainer Hillenbrand. Pseudoheterodyne detection for background-free near-field spectroscopy. *Appl. Phys. Lttr.*, 89(10):101124, 2006.